



INSTITUT DE FRANCE  
Académie des sciences

# Comptes Rendus

## Géoscience

### Sciences de la Planète

Ali Akbar Khezerlou, Michel Grégoire, Nasir Amel, Mohsen Moayyed, Ahmad Jahangiri and Mohammad Kilzi

**Whole rock and mineral chemistry of hornblenditic xenoliths in volcanic alkaline rocks from the northern part of Uromieh Dokhtar magmatic belt (NW Iran)**


Volume 353, issue S2 (2021), p. 187-215

<<https://doi.org/10.5802/crgeos.89>>

**Part of the Special Issue:** Perspectives on alkaline magmas

**Guest editor:** Bruno Scaillet (Institut des Sciences de la Terre d'Orléans, CNRS, France)

© Académie des sciences, Paris and the authors, 2021.  
*Some rights reserved.*

 This article is licensed under the  
CREATIVE COMMONS ATTRIBUTION 4.0 INTERNATIONAL LICENSE.  
<http://creativecommons.org/licenses/by/4.0/>



*Les Comptes Rendus. Géoscience — Sciences de la Planète sont membres du  
Centre Mersenne pour l'édition scientifique ouverte*  
[www.centre-mersenne.org](http://www.centre-mersenne.org)



---

Perspectives on alkaline magmas / *Perspectives sur les magmas alcalins*

# Whole rock and mineral chemistry of hornblenditic xenoliths in volcanic alkaline rocks from the northern part of Uromieh Dokhtar magmatic belt (NW Iran)

Ali Akbar Khezerlou<sup>Ⓜ</sup>\*,<sup>a</sup>, Michel Grégoire<sup>Ⓜ</sup><sup>b</sup>, Nasir Amel<sup>Ⓜ</sup><sup>a</sup>, Mohsen Moayyed<sup>Ⓜ</sup><sup>a</sup>, Ahmad Jahangiri<sup>Ⓜ</sup><sup>a</sup> and Mohammad Kilzi<sup>Ⓜ</sup><sup>b</sup>

<sup>a</sup> Department of Geology, University of Tabriz, Tabriz 51664, Iran

<sup>b</sup> Laboratory Geosciences Environnement Toulouse, Toulouse University, CNES-CNRS-IRD-UPS Midi-Pyrenees Observatory, 14 Av. E. Belin, 31400 Toulouse, France

*E-mails:* ali.khezerlou2@gmail.com (A. A. Khezerlou), michel.gregoire@get.omp.eu (M. Grégoire), n.Amel@Tabrizu.ac.ir (N. Amel), Moayyed@Tabrizu.ac.ir (M. Moayyed), a\_jahangiri@Tabrizu.ac.ir (A. Jahangiri), vtc\_oxytania\_vip@yahoo.com (M. Kilzi)

**Abstract.** An alkaline volcanic activity with a relative Plio-Quaternary age (based on the succession of layers on the field) occurred in the northern part of Uromieh Dokhtar magmatic belt, Iran. Hornblendite xenoliths mostly displaying cumulitic texture occur in the trachyandesites from this magmatic episode. The thermobarometric results indicate that these xenoliths formed within the crust. Based on mineralogical and chemical characteristics, these xenoliths are divided into two groups. In Group 1, plagioclase (andesine) modal content is less than 10% while amphibole (magnesian hastingsite) and biotite are the main minerals. In Group 2, plagioclase (labradorite) modal content is higher than 20% while amphibole (pargasite) and biotite are the main minerals. Positive anomalies of U, Ba, Ti, and K in hornblendite xenoliths are probably related to the accumulation process of amphibole and biotite. The study of the chemical composition of amphiboles indicates crystallization of amphibole from Group 1 and Group 2 hornblendite xenoliths and host volcanic rock under high oxidation conditions. Hornblendite xenoliths display high LREE/HREE and LREE/MREE ratios. The <sup>86</sup>Sr/<sup>87</sup>Sr ratios in xenoliths of Groups 1 and 2 and host volcanic rocks are 0.706291, 0.704685, and 0.709545, respectively, while <sup>143</sup>Nd/<sup>144</sup>Nd ratios are 0.512580, 0.512736, and 0.512561, respectively. Group 1 xenoliths are characterized by a negative Eu anomaly while this anomaly is positive for Group 2. Considering the REE concentrations and distribution patterns, the major element compositions of amphibole, biotite, and plagioclase as well as the Sr and Nd isotopic ratios, it appears that the parental melts of Group 1 and Group 2 xenoliths differ in composition. Those two theoretical parental melts also have different compositions when compared to that of the host volcanic rock. The studied alkaline rocks are commonly located along the main faults. Therefore it seems that the movement of the main faults (especially North Tabriz Fault, North Misho and Tasuj faults) has provided a path for the lavas carrying

---

\* Corresponding author.

the investigated xenoliths to penetrate the continental crust. Taken together the geochemical characteristics of the studied rocks indicate a mantle source variably metasomatized by a subduction event prior to the collision between Eurasian and Arabian continents.

**Keywords.** Hornblendite, Xenolith, Uromieh, Dokhtar, Iran.

Available online 23rd November 2021

## 1. Introduction

The Anatolian–Iranian plateau is one of the regions where active continent–continent collision is currently taking place. Previous studies to date [Sengor and Kidd, 1979, Dewey *et al.*, 1986] have shown that collision occurred between Eurasian and Arabian continents, resulting in the formation of an extensive (150,000 km<sup>2</sup>) high plateau with an average elevation of 2 km above sea level [Ahmadzadeh *et al.*, 2010]. The presence of potassium-rich volcanic rocks in this area is important, because these rocks occur in a variety of tectonic settings including continental convergent margins [Gill *et al.*, 2004], and syn- to post-collisional tectonic settings as in Anatolia and Tibet [Deng *et al.*, 2012, Conticelli *et al.*, 2013].

Alkaline rocks from this area contain various types of xenoliths, such as pyroxenite, gabbro, diorite and hornblendite xenoliths. Amphibole is frequently observed in xenoliths since it may occur in a wide range of pressure and temperature and is among the main constituents of mafic and ultramafic igneous and metamorphic rocks. Amphibole is moreover one of the most suitable minerals for thermobarometry estimates [Putirka, 2016].

Hornblende-rich xenoliths have been reported from several locations worldwide; e.g., northeast of Iran [Yousefzadeh and Sabzehei, 2012], central Mexico [Blatter and Carmichael, 1998], Iberian Peninsula [Capedri *et al.*, 1989], western and central Europe [Downes *et al.*, 2001, 2002, Carraro and Visonà, 2003], and central Spain [Orejana *et al.*, 2006]. The majority of the hornblendite xenoliths are related to the host volcanic rocks [Witt-Eickschen and Kramm, 1998] while some others are witnesses of a metasomatized mantle or cumulates from older magmatic events [e.g., Frey and Prinz, 1978, Irving, 1980, Capedri *et al.*, 1989, Saadat and Stern, 2012, Rajabi *et al.*, 2014, Su *et al.*, 2014, Kheirkhah *et al.*, 2015].

In the study area, volcanic rocks have been previously investigated in terms of their geochemistry and petrology by Khezerlou *et al.* [2008] and Ahmadzadeh *et al.* [2010]. Moreover, pyroxenite

[Khezerlou *et al.*, 2017], gabbro and diorite xenoliths [Khezerlou *et al.*, 2020] have been studied in terms of their geochemistry, isotope, and mineralogy. Studies of volcanic rocks and xenoliths in the study area have shown that their constituent magmas originate from a metasomatized mantle. However, no such information is available about the hornblendite xenoliths. Studying hornblende-rich rocks occurring in volcanic rocks can provide valuable information about their origin and the magmatic history of the investigated area. Hence, the present research was conducted to investigate the petrographic and geochemical characteristics of the hornblendite xenoliths and their host volcanic rocks from the northern part of Uromieh Dokhtar magmatic belt. Moreover, major and trace element data, and <sup>143</sup>Nd/<sup>144</sup>Nd and <sup>86</sup>Sr/<sup>87</sup>Sr isotopic ratios were evaluated to determine the petrogenesis, and establish the relationship between the magmatic source of these xenoliths and their host volcanic rocks.

## 2. Geological setting

The Neotethys subduction process that occurred beneath Central Iran during the upper Cretaceous and Paleogene and the collision process between the Iran and Arabia Platforms created four structural zones in Iran. These zones are; the High Zagros belt, the Sanandaj–Sirjan zone, the Uromieh Dokhtar magmatic belt, and the Zagros folded zone [Alavi, 2004]. The study area is located in the northernmost of the Uromieh Dokhtar magmatic belt, characterized by a magmatic activity which started during the late Cretaceous and was active from Eocene to Quaternary. The peak magmatism of this zone occurred during Eocene [Farhoudi, 1978, Emami, 1981, Alavi, 2004]. However, it ceased for a short time and started again during the upper Miocene to Plio-Quaternary [Omranian *et al.*, 2008]. The volcanic rocks from the northwest of Marand overlie the Upper Miocene clastic and evaporitic rocks, being possibly Plio-Quaternary in age.

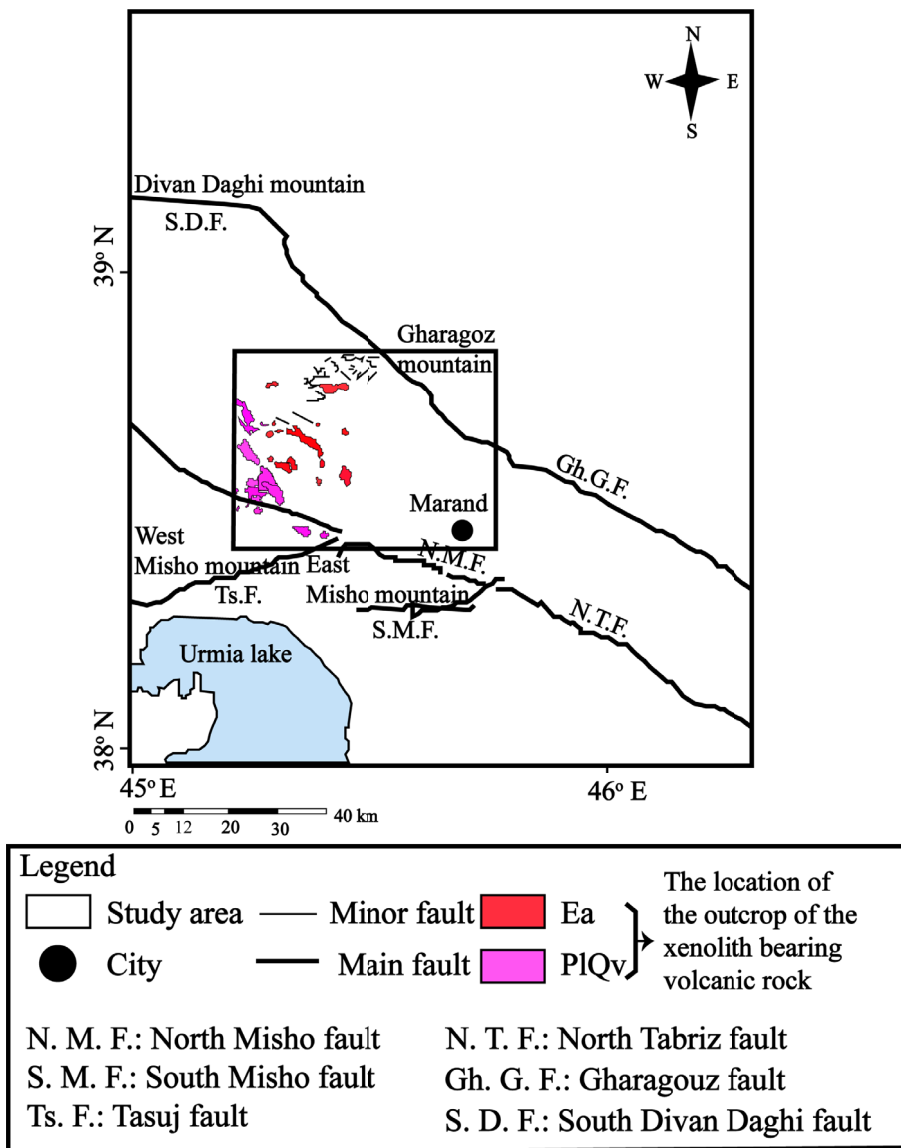


**Figure 1.** Tectonic map of the investigated area, showing the location of the outcrop of the xenoliths-bearing volcanic rocks [modified after Khezerlou *et al.*, 2020]. Ea (Eocene, pyroxine andesite)–PIQv (Plio-Quaternary, volcanic).

The study area is located between the main faults of the region including North Tabriz (N. T. F), Misho (N. M. F and S. M. F), and Tasuj (Ts. F) faults to the south and Garagouz (Gh. G. F) and South Divan Daghi (S. D. F) faults to the north (Figure 1).

Field surveys revealed a wide range of volcanic and volcanoclastic rocks outcropping in this area (Figure 2). The volcanoclastic rocks from the study area include agglomerate, breccia, and tuff litholo-

gies. The volcanic rocks of the study area are identified in Figure 2 by PLQv (trachyandesite) and Ea (pyroxene andesite) acronyms. In detail, in the area of PLQv, the volcanic rocks also include basanite, tephrite, and basalt trachyandesites, in addition to trachyandesite which is the dominant rock type. There are also tuffs in this area which are in contact with trachyandesite volcanic rocks. In some locations, 2–3 m thick layers of volcanic ashes with a

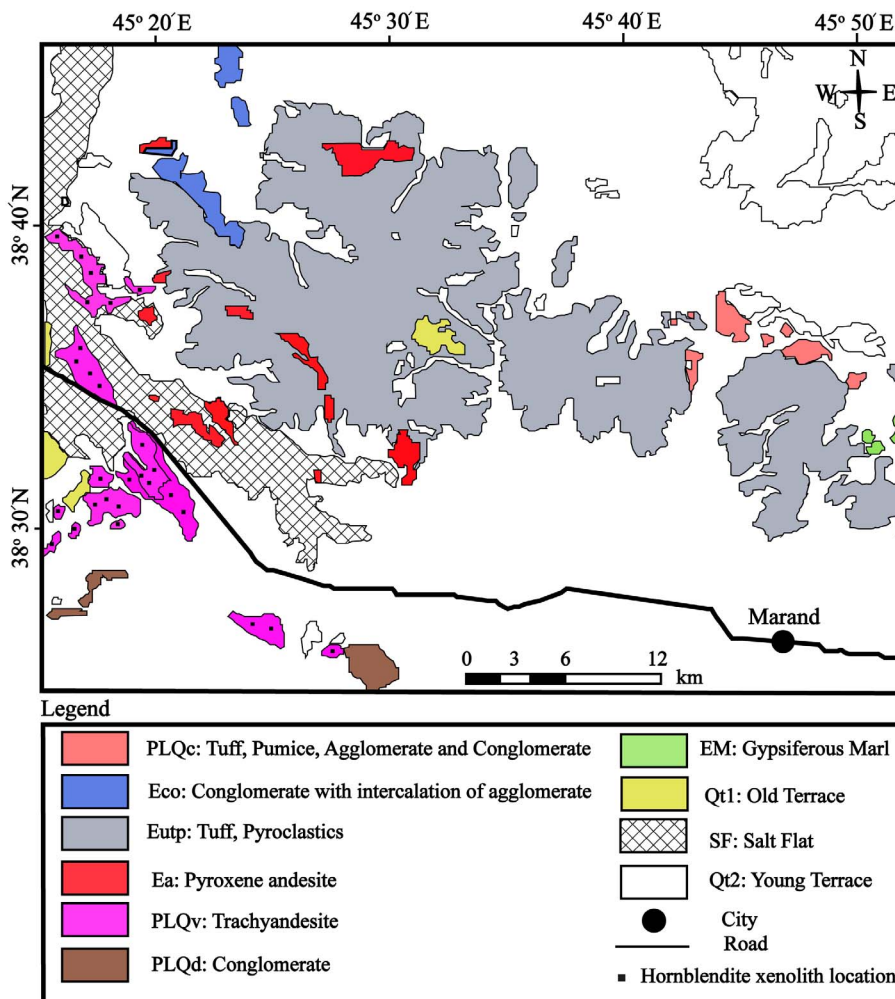


**Figure 2.** Geological map of the investigated area. (Simplified from the 1:100,000 geological maps of Marand, Jolfa, Gharezaadin and Tasuj) [modified after Khezerlou *et al.*, 2017]. Location of sampling includes Ea and PLQv.

trachyandesite composition are observed in contact with tuffs [Khezerlou *et al.*, 2008]. Xenoliths occurring in this area (PLQv) are gabbros, diorites, hornblendites, lamprophyres, and pyroxenites hosted by trachyandesites and basalt trachyandesites. In the area of Ea (pyroxene andesite), the volcanic rocks include leucitite, leucite–basanite, leucite–tephrite, basanite, tephrite, basalt trachyandesites, trachydacite, and dacite. Xenoliths occurring in this area (Ea) are gabbros, diorites, and pyroxenites hosted by basalt trachyandesites.

Several dykes outcrop in the study area. They are mostly ultrapotassic in composition. Also, some lamprophyric dykes between 9 and 11 Ma (Late Miocene)

in age occur in the study area in Sorkheh, Iran [Ag-hazadeh *et al.*, 2015].

In the southern part of the study area, in the Misho Mountain (Southwest of Marand), some outcrops of mafic rocks including gabbro, diorite, anorthosite and olivine gabbro occur, sometimes associated to ultrabasic rocks ranging from peridotite to highly serpentinized pyroxenite. These rocks are located above the Kahar Formation, and are covered by a weathering shell. Thus, their relative age is estimated to be younger than that of the Kahar Formation and older than the Permian [Azimzadeh, 2013]. In this regard, Saccani *et al.* [2013] ascribe these rocks to the Paleotethys. There

is also a granitoid mass in the Misho Mountain (southwest of Marand), along with intermediate and acidic rocks including diorite, tonalite, monzogranite, granodiorite, and granite, which are S-type granitoids with a potassic calc-alkaline affinity, and which crop out near the Misho gabbros [Shahzeidi, 2013].

### 3. Analytical methods

The major element compositions of minerals were acquired at the “Centre de Micro Caractérisation Raimond Castaing” (CNRS, University Toulouse III, INPT, INSA, Toulouse, France), using a Cameca SX-Five electron microprobe. The operating conditions were as follows: accelerating voltage 15 kV; beam current 20 nA; analysed surface around  $2 \times 2 \mu\text{m}^2$ . The following standards were used: albite (Na), periclase (Mg), corundum (Al), sanidine (K), wollastonite (Ca, Si), pyrophanite (Mn), hematite (Fe),  $\text{Cr}_2\text{O}_3$  (Cr), NiO (Ni) and sphalerite (Zn).

The bulk rock major and minor elements were analyzed using an Inductively Coupled Plasma Atomic Emission Spectrometer (ICP-AES) Horiba Jobin Yvon Ultima 2 at the “Pôle de Spectrométrie Océan” (PSO/IUEM, Plouzané, France), following the protocol adapted from Cotten *et al.* [1995]. Each powdered sample was digested in Teflon vials with HF 32N and  $\text{HNO}_3$  14.4N and the dry residue was dissolved in a  $\text{H}_3\text{BO}_3$  solution. WSE and ACE international standards were used as internal and external control. The precision of measurements performed on that instrument is usually better than 1% for both  $\text{SiO}_2$  and  $\text{TiO}_2$ , 2% for  $\text{Al}_2\text{O}_3$  and  $\text{Fe}_2\text{O}_3$ , and better than 4% for the other major oxides.

Trace element concentrations were determined using a High Resolution Inductively Coupled Plasma Mass Spectrometer (HR ICP-MS) Thermo Finnigan Element II (“Pôle de Spectrométrie Océan” PSO/IUEM, Plouzané, France), following a method adapted from Barrat *et al.* [2007]. About 100 mg of sample were digested in Teflon vials within distilled HF 32N and  $\text{HNO}_3$  14.4N. The dry residue was dissolved in  $\text{HNO}_3$  14.4N and then in HCl 3N. An aliquot of the solution was diluted in  $\text{HNO}_3$  0.3N and spiked with Tm spike. BCR2 and BEN were used as external control and BHVO-2 was used for internal control. The precision of measurements was better than 5% for all elements.

Samples were also analyzed for Sr and Nd radiogenic isotopes. About 200 mg of sample material was weighed and dissolved in Savillex beakers in a mixture of ultrapure distilled HF (24N), and  $\text{HNO}_3$  (14N) for four days at 120 °C on a hot plate. Sr and Nd fractions were chemically separated using the Eichrom specific resins TRU-spec, Sr-spec and Ln-spec following conventional column chemistry procedure [Pin and Santos Zalduegui, 1997]. The Sr and Nd isotope compositions were measured in static mode on a Thermo TRITON spectrometer at the PSO (IUEM, Plouzané, France). All measured Sr and Nd ratios were normalized to  $^{86}\text{Sr}/^{88}\text{Sr} = 0.1194$  and  $^{146}\text{Nd}/^{144}\text{Nd} = 0.7219$ , respectively and  $^{87}\text{Sr}/^{86}\text{Sr}$  values were normalized to the recommended value of NBS987 (0.710250). During the course of analysis, Nd standard solution La Jolla gave  $0.511859 \pm 2$  ( $n = 2$ , recommended value 0.511850) and JNdi gave  $0.512117 \pm 3$  ( $n = 1$ , recommended value 0.512100).

### 4. Petrography

#### 4.1. Host volcanic rocks

The volcanic series of the study area consists of  $\text{SiO}_2$ -undersaturated rocks (e.g., leucitite, leucite-basanite, leucite-tephrite, basanite, and tephrite) to  $\text{SiO}_2$ -saturated rocks such as trachyandesite, andesite, trachydacite, and dacite. The hornblendite xenoliths occur within the trachyandesite rocks. These rocks show microlitic porphyritic (Figure 3a) or porphyritic (Figure 3d) textures.

Andesine plagioclase is the most abundant mineral phase in these volcanic rocks, making 45–50% of total modal content. The size of this mineral varies from very fine microliths (less than 0.1 mm) occurring within the matrix, to phenocrysts up to 1.2 mm in size. In some cases, the variation in size is transitional, resulting in a seriate texture (Figure 3a). Most of the plagioclases display Carlsbad and polysynthetic twins and some of them display a sieve texture (Figure 3a) or even zoning (Figures 3a, d). Clinopyroxene constitutes 8–10% of the samples. This mineral is observed as phenocryst in the investigated rocks but not as microlite in the matrix. It is euhedral to subhedral and ranges in size from 0.2 to 1.5 mm. The minor mineral phases of these rocks include amphibole, biotite, K-feldspar, apatite, and opaque minerals associated to glass in some samples. Euhedral and subhedral brown hornblende ranging in size from 0.2 to



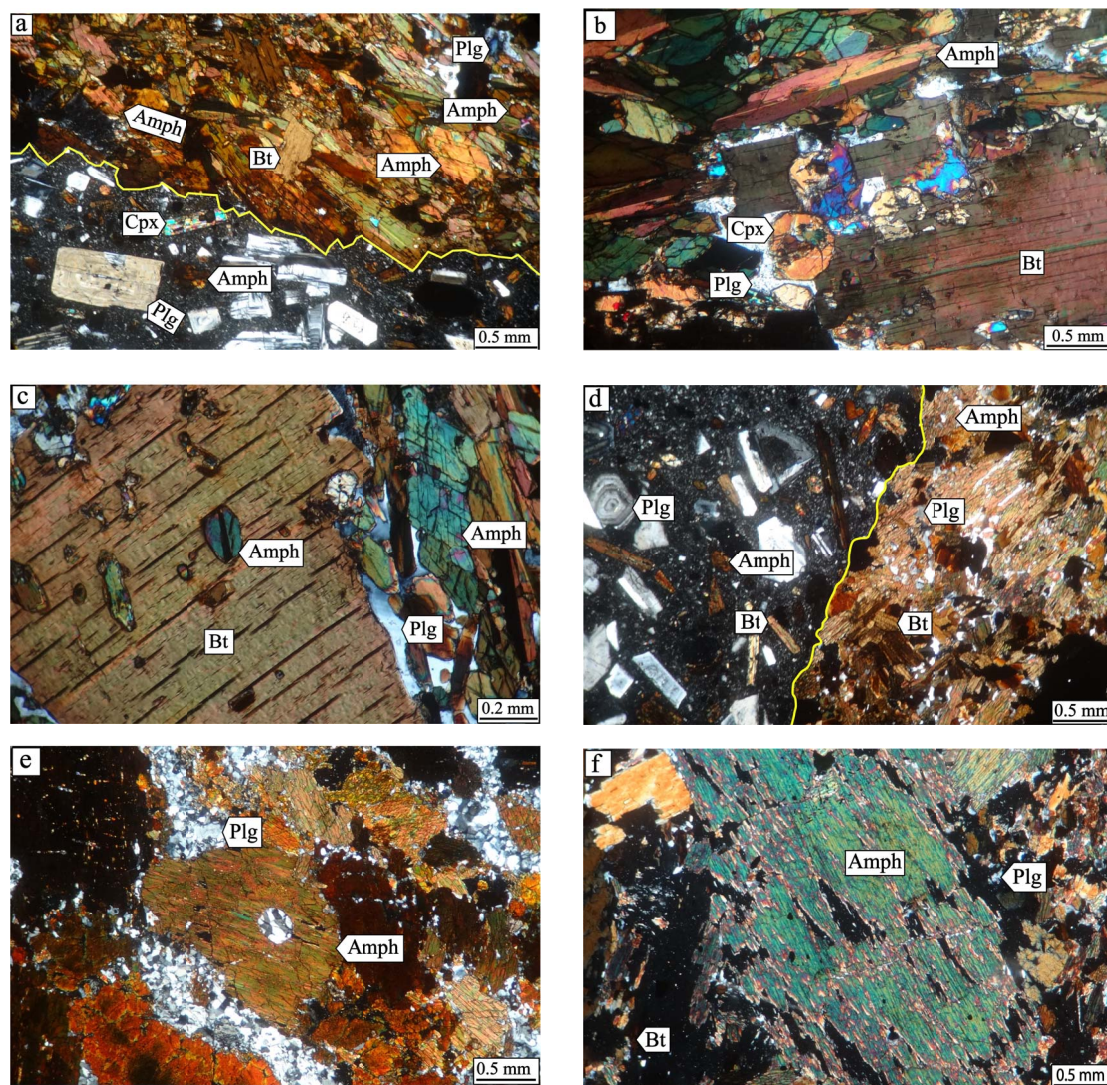


**Figure 3.** Photomicrographs of host volcanic rocks and hornblende xenoliths from the study area: (a) plagioclase (Plg), clinopyroxene (Cpx), amphibole (Amph) and biotite (Bt) phenocrysts in trachyandesite and hornblende with amphibole and biotite as cumulus phases and plagioclase as intercumulus phase (crossed polars: XPl). (b) Hornblende with amphibole, clinopyroxene and biotite as cumulus phases and plagioclase as intercumulus phase, XPl. (c) Hornblende with amphibole and biotite as cumulus phases and plagioclase as intercumulus phase, XPl. (d) Plagioclase, amphibole and biotite phenocrysts in trachyandesite and hornblende with amphibole and biotite as cumulus phases and plagioclase as intercumulus phase, XPl. (e) Hornblende with amphibole (as cumulus phase) and plagioclase as intercumulus phase, XPl. (f) Hornblende with amphibole and biotite as cumulus phases and plagioclase as intercumulus phase, XPl. Group 1 xenolith: a–c. Group 2 xenolith: d–f.

1 mm is also observed, amounting up to 4–5% of the modal content of samples, some crystals displaying opacitization (Figure 3a). Another minor mineral is

biotite, which makes up to 4–6% of the mode. The size of this mineral ranges from 0.3 to 0.8 mm, and some biotites also display opacitization (Figure 3d).

Apatite and opaque minerals smaller than 0.5 mm (1–2% of the mode) commonly occur.

#### 4.2. Hornblendite xenoliths

Hornblendite xenoliths are elliptic black lustrous rock pieces with dimensions of 3 × 10 cm. Based on the occurrence or absence of clinopyroxene and the plagioclase modal content, these xenoliths are divided into two groups: Group 1 with clinopyroxene and always less than 10% of plagioclase and Group 2 lacking clinopyroxene and with commonly more than 10% of plagioclase.

##### 4.2.1. Group 1

Amphibole constitutes 65–80% of the modal content of hornblendites from this group. Biotite and plagioclase are the two other main mineral phases with modal content ranging from 5 to 25% and from 5 to 10%, respectively (Table 7). These rocks are characterized by adcumulus texture with 0.2–0.35 mm subhedral to euhedral brown amphibole as the main cumulus phase (Figures 3a–c). In some amphiboles of this group, a slight color change is seen from the mantle to the rim, so that the color of the rim looks darker than the mantle (Figure 3a). Euhedral and subhedral biotites ranging from 0.5 to 3 mm in size also occur as cumulus phases in these samples. Biotite in this group is more abundant than in Group 2 hornblendite xenoliths and host volcanic rocks. Some samples locally show a poikilitic texture, characterized by tiny opaques and amphiboles included within biotite crystals (Figure 3c). Small anhedral plagioclases constitute the intercumulus phase. Clinopyroxene, opaque, and apatite are minor minerals in Group 1 samples. Clinopyroxene mostly occurs as subhedral crystals less than 1 mm in size (Figure 3b).

##### 4.2.2. Group 2

Group 2 hornblendites display orthocumulus texture (Figures 3d–f) with amphibole (55–95%), plagioclase (3–25%), and biotite (3–12%) as the main mineral phases (Table 7). Similar to the Group 1 xenoliths, amphibole and biotite are the cumulus phases while plagioclase is the intercumulus phase. Amphiboles in this group are euhedral and subhedral and range from 0.2 to 5.5 mm. Amphiboles are more abundant in this group compared to the

Group 1 xenoliths and host volcanic rocks, and show no distinct orientation (Figures 3d–f). Biotites are mainly subhedral and 0.5–3 mm in size and are less abundant compared to Group 1. Moreover, 0.2–1 mm large anhedral plagioclases occur in the interstices of these mafic minerals. Unlike the Group 1 xenoliths and host volcanic rocks, this group does not contain clinopyroxene. Opaque minerals and apatite less than 1 mm in size are observed as minor minerals in this group. They are less abundant than in Group 1 hornblendites.

## 5. Results and discussion

### 5.1. Mineral chemistry

Four samples were analyzed using the electron microprobe technique (two samples from Group 1, one from Group 2 and one from host volcanic). For samples k (v-k), k-6 (v-k-6) and k-8 (v-k-8), the constituent minerals of the host volcanic rock (v-k, v-k-6 and v-k-8) and xenoliths (k, k-6 and k-8) were analyzed, while for sample v-k-20 only the constituent minerals of the host volcanic rock were analyzed.

#### 5.1.1. Clinopyroxene

As mentioned above, Group 2 hornblendite xenoliths lack clinopyroxene and thus for comparison, some clinopyroxene of the host volcanic rocks and Group 1 hornblendite xenoliths are presented, in order to determine differences or similarities of composition, magmatic series and conditions of formation of this mineral in the studied samples.

The composition of clinopyroxenes in Group 1 hornblendite xenoliths and host volcanic rocks plot in the field of Quad (Ca-pyroxene) in the Q–J diagram of Morimoto and Kitamura [1983] (Figure 4a). All the investigated clinopyroxenes are diopsides (Figure 4b).

The composition of clinopyroxenes can provide valuable information about the magmas from which they crystallized [Zhang *et al.*, 2018]. The Ti versus Ca+Na diagram [Leterrier *et al.*, 1982] indeed shows that clinopyroxenes from host volcanic rocks lie in the alkaline field and clinopyroxenes from Group 1 hornblendite xenoliths lie in the alkaline field and close to the dividing line (Figure 4c). The position of all investigated clinopyroxenes of host volcanic rocks in the Na+Al<sup>IV</sup> versus Cr+2Ti+Al<sup>VI</sup> diagram



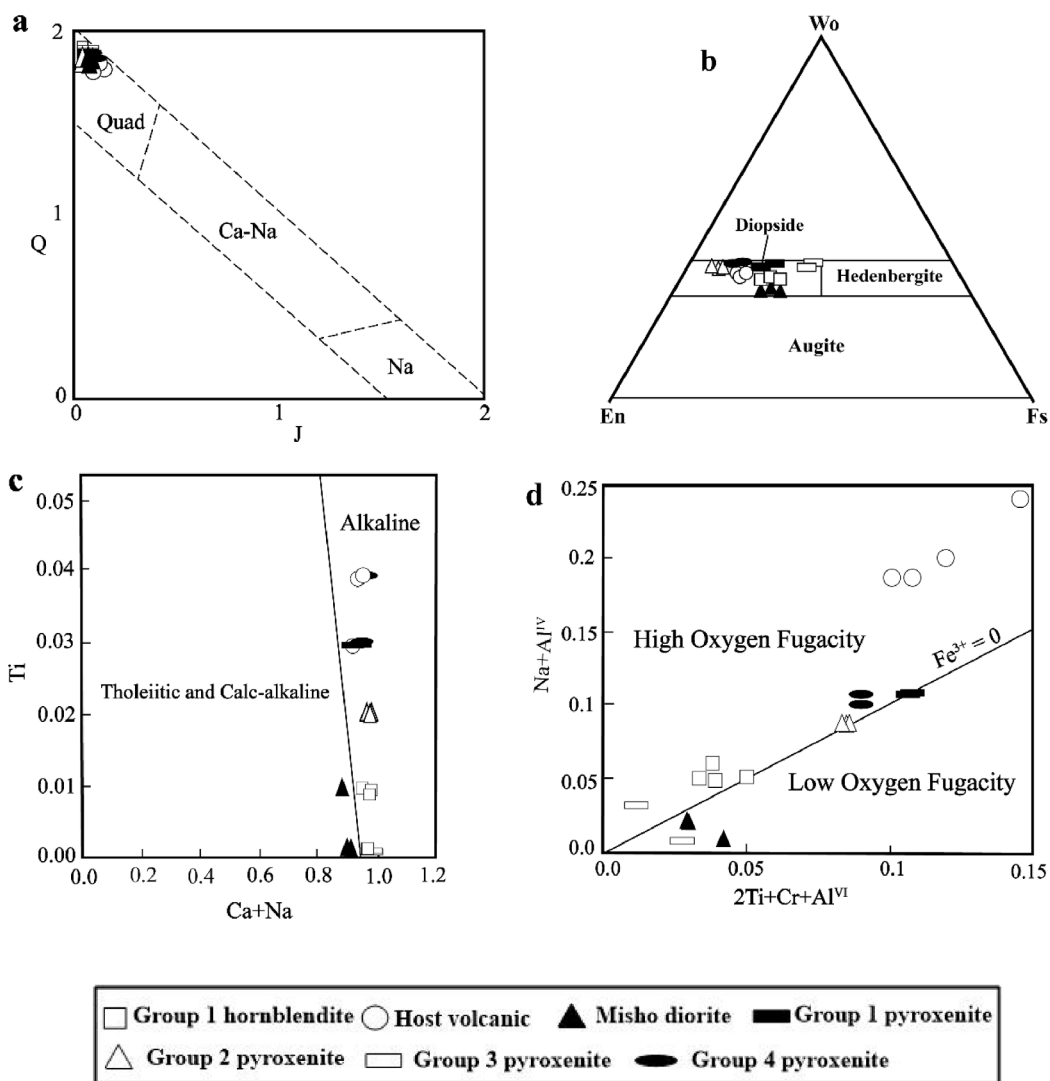


**Figure 4.** (a) Composition of clinopyroxenes in the Q–J diagram ( $J = 2Na$ ,  $Q = Ca + Mg + Fe^{2+}$ ) [Morimoto and Kitamura, 1983]. (b) Classification of clinopyroxenes [Morimoto *et al.*, 1988]. (c) Plot of Ti versus  $Na + Ca$  for clinopyroxenes from the volcanic rocks and Group 1 hornblende xenoliths [Leterrier *et al.*, 1982]. (d) Plot of  $Na + Al^{IV}$  versus  $2Ti + Cr + Al^{VI}$  for clinopyroxenes from the samples [Schweitzer *et al.*, 1979].

[Schweitzer *et al.*, 1979] indicates that they crystallized at high oxygen fugacity conditions (Figure 4d). The clinopyroxenes of Group 1 hornblende xenoliths in this diagram plot also in the high oxygen fugacity field, close to the dividing line, with a sample plotting on the dividing line. The  $Mg/Mg + Fe^{2+}$  of clinopyroxenes from Group 1 hornblende xenoliths and host volcanic rocks varies from 0.73 to 0.74 and 0.82 to 0.84, respectively (Table 1).

Figure 4b illustrates the compositional difference between clinopyroxenes from Group 1 hornblende xenoliths and those from volcanic rocks. Clinopyroxenes from Group 1 hornblende xenoliths indeed display higher  $SiO_2$  and  $MnO$  contents and lower  $Al_2O_3$ ,  $TiO_2$ , and  $Na_2O$  contents than those of clinopyroxene from their host volcanic rocks. In order to compare the composition of clinopyroxenes from Group 1 hornblende xenoliths with groups 1,

**Table 1.** Mineral chemical composition of clinopyroxenes in hornblendite xenoliths, host volcanic rocks and Misho diorites

Mineral Rock Sample Location	Clinopyroxene										
	Group 1 xenolith				Host volcanic				Misho diorite		
	k	k	k	k	v-k	v-k	v-k	v-k	A2-43	A2-43	A2-43
Core	Core	Core	Core	Core	Core	Core	Core	Core	Core	Core	
SiO <sub>2</sub>	52.57	52.93	52.83	52.75	49.44	49.21	46.85	48.54	54.02	53.86	54.34
TiO <sub>2</sub>	0.20	0.18	0.21	0.19	1.21	1.23	1.28	1.27	0.17	0.19	0.13
Al <sub>2</sub> O <sub>3</sub>	0.92	0.97	1.10	1.11	3.83	3.84	6.21	3.99	0.58	0.63	0.72
Cr <sub>2</sub> O <sub>3</sub>	0.01	0.00	0.00	0.02	0.01	0.01	0.02	0.01	0.00	0.05	0.04
FeO(t)	8.59	8.77	9.40	8.92	7.94	8.75	9.13	8.33	10.74	10.65	10.18
MnO	0.70	0.72	0.73	0.71	0.45	0.39	0.37	0.41	0.19	0.21	0.26
MgO	13.07	12.88	12.67	12.95	13.18	12.71	11.75	12.72	13.61	13.65	13.05
CaO	22.80	22.75	23.28	22.94	22.39	22.42	22.65	22.23	21.58	21.75	22.42
Na <sub>2</sub> O	0.39	0.48	0.46	0.42	0.63	0.65	0.61	0.71	0.21	0.20	0.14
K <sub>2</sub> O	0.00	0.00	0.00	0.00	0.00	0.00	0.02	0.02	0.00	0.00	0.02
Total	99.25	99.66	100.69	100.01	99.08	99.21	98.89	98.23	101.10	101.19	101.30
Cations calculated on the basis of 6 oxygens											
Si	1.98	1.99	1.97	1.98	1.87	1.87	1.79	1.86	2.00	1.99	2.01
Al <sup>IV</sup>	0.02	0.01	0.03	0.02	0.13	0.13	0.21	0.14	0.00	0.01	0.00
Al <sup>VI</sup>	0.02	0.03	0.02	0.03	0.04	0.04	0.07	0.04	0.03	0.02	0.04
Fe <sup>3+</sup>	0.02	0.01	0.04	0.03	0.10	0.11	0.16	0.13	0.00	0.00	0.00
Cr	0.00	0.00	0.00	0.00	0.00	0.00	0.00	0.00	0.00	0.00	0.00
Ti	0.01	0.00	0.01	0.01	0.03	0.04	0.04	0.04	0.00	0.01	0.00
Fe <sup>2+</sup>	0.25	0.26	0.25	0.25	0.15	0.16	0.12	0.13	0.33	0.33	0.32
Mn	0.02	0.02	0.02	0.02	0.01	0.01	0.01	0.01	0.01	0.01	0.01
Mg	0.73	0.72	0.71	0.72	0.74	0.72	0.67	0.73	0.75	0.75	0.72
Ca	0.92	0.91	0.93	0.92	0.91	0.91	0.93	0.91	0.86	0.86	0.89
Na	0.03	0.03	0.03	0.03	0.05	0.05	0.05	0.05	0.02	0.01	0.01
K	0.00	0.00	0.00	0.00	0.00	0.00	0.00	0.00	0.00	0.00	0.00
Total	4.01	4.00	4.01	4.01	4.03	4.04	4.05	4.04	3.99	3.99	3.98
mg#	0.74	0.73	0.74	0.74	0.84	0.82	0.84	0.84	0.69	0.70	0.69
Wo	47.26	47.32	47.70	47.33	47.41	47.52	48.90	47.62	43.98	44.17	45.97
En	37.71	37.28	36.12	37.18	38.83	37.49	35.30	37.91	38.59	38.58	37.23
Fs	15.02	15.40	16.18	15.49	13.76	14.99	15.81	14.47	17.43	17.25	16.80

Misho data are from Shahzeidi [2013].

2, 3 and 4 of pyroxenite xenoliths from study area [Khezerlou *et al.*, 2017], representative analyses of the latter are given in Figures 4a–d. As can be seen in these figures, the compositions of the clinopyroxenes from Group 1 hornblendite xenoliths differ from those of clinopyroxenes from pyroxenite xenoliths of

the study area. They are different in most of the major elements such as SiO<sub>2</sub>, Na<sub>2</sub>O, MgO, FeO(t), MnO, and Al<sub>2</sub>O<sub>3</sub> (Table 1). We also compared the clinopyroxenes from the xenoliths with those from the Misho diorites, located near the study area [Shahzeidi, 2013]. In both cases the clinopyroxenes are diopsides

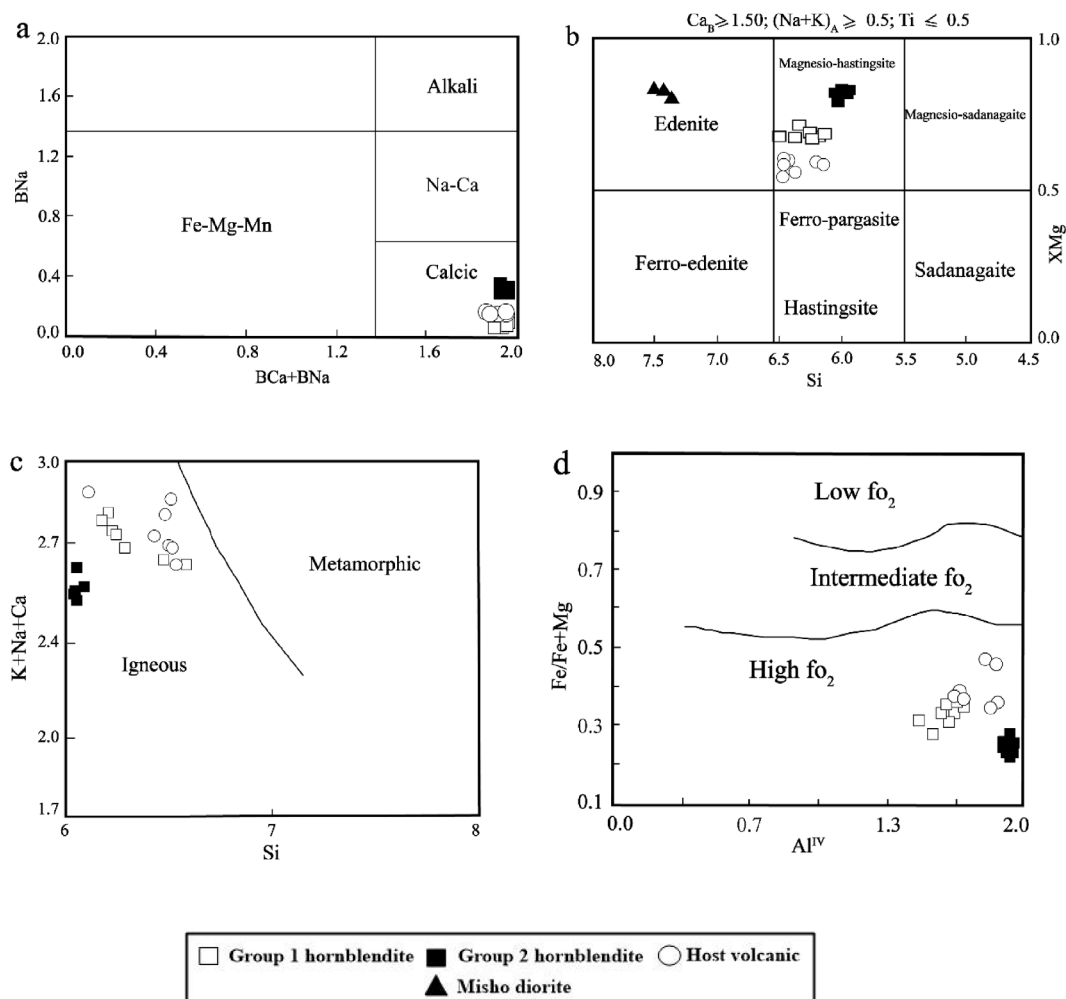


**Figure 5.** (a) Composition of amphiboles in the BCa+BNa versus BNa diagram [Leake *et al.*, 1997]. (b) Classification of amphiboles [Leake *et al.*, 1997]. (c) Plot of Si versus K+Na+Ca for amphiboles from the investigated samples [Sial *et al.*, 1998]. (d) Plot of Al<sup>IV</sup> versus Fe/Fe+Mg for amphiboles from the host volcanic rocks and hornblende xenoliths [Anderson and Smith, 1995].

(Figure 4b) but those from Group 1 hornblende xenoliths contain more Al<sub>2</sub>O<sub>3</sub>, CaO, MnO, and Na<sub>2</sub>O and less SiO<sub>2</sub> and FeO compared to those from the Misho diorites (Table 1). As can be seen in Figures 4c and d, the composition of the clinopyroxenes from Group 1 hornblende xenoliths differs from those of clinopyroxenes from the Misho diorites.

### 5.1.2. Amphibole

As shown in Figure 5a, the amphiboles from all the investigated xenoliths (Group 1 and Group 2) as well as amphiboles from host volcanic rocks are

calcic amphiboles as illustrated by the BNa versus BNa+BCa diagram of Leake *et al.* [1997]. More precisely, according to Mg/Mg+Fe<sup>2+</sup> versus Si diagram [Leake *et al.*, 1997], amphiboles from Group 1 xenoliths and host volcanic rocks are magnesianhastingsites while those from Group 2 hornblende xenoliths are pargasites (Figure 5b). In the K+Na+Ca versus Si diagram [Sial *et al.*, 1998], amphiboles from the two groups of hornblende xenoliths plot within the magmatic (igneous) amphiboles field (Figure 5c).

The Mg/Mg+Fe<sup>2+</sup> ratio of amphibole from Group 1 and Group 2 xenoliths and host volcanic

rocks vary from 0.67 to 0.72, 0.79 to 0.85, and 0.54 to 0.67, respectively (Table 2). In the  $Al^{IV}$  versus  $Fe^{2+}/Fe^{2+}+Mg$  diagram [Anderson and Smith, 1995], amphiboles from the xenoliths and host volcanic rocks fall within the high-oxygen fugacity field (Figure 5d). The core, mantle and rim of amphiboles from Group 2 hornblende xenoliths do not show considerable and systematic change in composition. Yet, in some of amphiboles of Group 1,  $FeO(t)$ ,  $CaO$  and  $MnO$  increase from the mantle to the rim (Table 2).

As shown in Figure 5b, the amphiboles of the host volcanic rock and those of the two groups of hornblende xenoliths display some compositional differences; for instance, amphiboles from Group 1 and Group 2 xenoliths show higher  $MgO$  and  $Mg/Mg+Fe^{2+}$  values and lower  $FeO(t)$ ,  $K_2O$ , and  $MnO$  (and also  $Al_2O_3$  for Group 2) contents than those of their equivalent in host volcanic rocks. Furthermore, some differences also occur between amphiboles from the two groups of hornblende xenoliths; for instance, amphiboles from Group 1 have slightly higher  $TiO_2$ ,  $Na_2O$ ,  $MgO$ , and  $CaO$  contents and a lower  $Al_2O_3$  content than amphibole from Group 2 (Table 2). The composition of amphiboles between different samples (k, k-6) in Group 1 hornblende xenoliths is not homogeneous and there is a slight difference in the content of some of the major elements (for example,  $SiO_2$ ,  $Al_2O_3$ ,  $K_2O$ ) (Table 2).

We also compared the amphiboles of the two investigated groups of hornblende xenoliths with those of the Misho diorites [Shahzeidi, 2013]. Amphiboles in the Misho diorites are edenites (Figure 5b), and are different from those from the investigated hornblende xenoliths in terms of major elements such as  $SiO_2$ ,  $TiO_2$ ,  $Na_2O$ ,  $MgO$ ,  $K_2O$ ,  $FeO(t)$ ,  $MnO$ , and  $Al_2O_3$  (Table 2).

### 5.1.3. Feldspar

According to the classification of Deer *et al.* [1966], the composition of plagioclases in Group 1 and Group 2 hornblende xenoliths is andesine and labradorite, respectively. On the other hand, the composition of feldspars of their host volcanic rocks are oligoclase, andesine and sanidine (Figure 6). Zoning occurs in some volcanic plagioclase phenocrysts, with  $SiO_2$ ,  $Na_2O$ , and  $K_2O$  contents increasing from rim to core while  $CaO$  and  $Al_2O_3$  contents decrease (normal zoning) (Table 3).

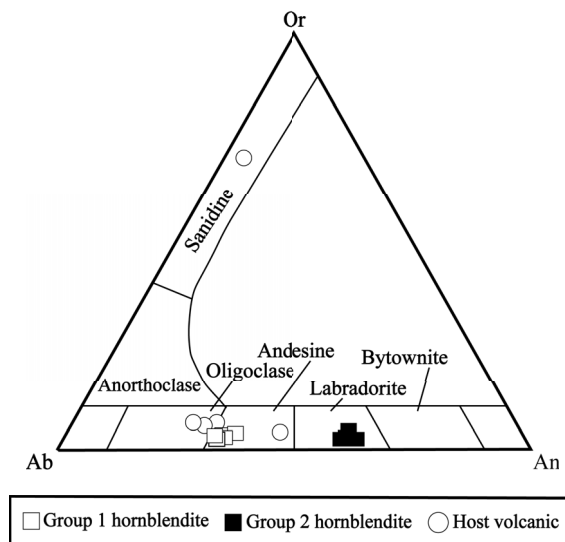


**Figure 6.** Classification of plagioclases from the host volcanic rocks and hornblende xenoliths [Deer *et al.*, 1966].

### 5.1.4. Biotite

According to the  $Al^{IV}$  versus  $Fe^{2+}/Fe^{2+}+Mg$  diagram, micas from Group 1 and Group 2 hornblende xenoliths and host volcanic rocks are biotites (Figure 7a) with  $Mg/Mg+Fe^{2+}$  values ranging from 0.62 to 0.66, 0.64 to 0.65 and 0.60 to 0.61, respectively (Table 4).

The ternary diagram  $MgO-Fe+MnO-10TiO_2$  can be used to assess the origin of micas [Nachit *et al.*, 2005] which suggests that biotites from Group 1 hornblende xenoliths and host volcanic rocks are primary magmatic micas while those from Group 2 hornblende xenoliths are recrystallized type (Figure 7b).

The biotites from Group 2 hornblende xenoliths do not display compositional variation from core to rim (Table 4), similarly to amphiboles and plagioclases. Biotites in Group 1 hornblende xenoliths display cores respectively higher in  $Al_2O_3$ ,  $SiO_2$ , and  $CaO$  and lower in  $MgO$ ,  $FeO$ , and  $K_2O$  than their rims (Table 4). The compositions of biotites from Group 1 and Group 2 hornblende xenoliths are different (Figure 7a). Biotites from Group 1 hornblende xenoliths have higher  $SiO_2$  and  $TiO_2$  contents and lower  $MgO$ ,  $MnO$ , and  $Na_2O$  compared to micas of Group 2 (Table 4). The results show that biotites of Group 1 hornblende xenoliths are also

**Table 2.** Mineral chemical composition and *P–T* estimate of amphiboles in hornblendite xenoliths, host volcanic rocks and Misho diorites

Mineral	Amphibole										
	Rock	Group 1 xenolith						Misho diorite			
Sample	k	k	k	k-6	k-6	k-6	k-6	k-6	A2-43	A2-43	A2-43
Location	Core	Core	Core	Rim 1	Mantle 1	Core	Mantle 2	Rim 2	Core	Core	Core
SiO <sub>2</sub>	43.52	43.21	43.31	42.74	42.63	42.11	42.00	42.08	52.57	53.61	52.89
TiO <sub>2</sub>	1.82	2.15	2.07	2.13	2.16	2.24	2.26	2.18	0.15	0.14	0.23
Al <sub>2</sub> O <sub>3</sub>	10.68	11.75	11.78	12.26	12.26	12.56	12.57	12.39	3.54	3.51	3.78
Cr <sub>2</sub> O <sub>3</sub>	0.01	0.02	0.00	0.02	0.00	0.00	0.01	0.02	0.03	0.01	0.03
FeO(t)	12.27	12.72	11.82	12.98	12.71	12.74	12.82	13.36	15.30	14.48	15.80
MnO	0.13	0.23	0.13	0.20	0.10	0.15	0.10	0.20	0.28	0.02	0.32
MgO	12.68	12.48	13.40	12.81	12.71	12.53	12.63	12.40	14.57	15.49	14.57
CaO	11.47	11.67	11.76	12.08	11.78	11.81	11.98	11.99	10.92	10.75	10.27
Na <sub>2</sub> O	1.99	2.20	2.23	2.32	2.17	2.24	2.23	2.22	0.33	0.28	0.42
K <sub>2</sub> O	1.08	1.05	0.95	1.10	1.13	1.16	1.24	1.16	0.25	0.19	0.22
Total	95.64	97.46	97.47	98.63	97.65	97.53	97.84	98.00	97.94	98.48	98.53
Cations calculated on the basis of 23 oxygens											
Si	6.52	6.37	6.35	6.25	6.27	6.22	6.19	6.21	7.46	7.49	7.41
Al <sup>IV</sup>	1.48	1.63	1.65	1.75	1.73	1.78	1.81	1.79	0.54	0.51	0.59
Sum T	8.00	8.00	8.00	8.00	8.00	8.00	8.00	8.00	8.00	8.00	8.00
Al <sup>VI</sup>	0.41	0.42	0.38	0.36	0.40	0.40	0.38	0.36	0.05	0.07	0.04
Ti	0.21	0.24	0.23	0.23	0.24	0.25	0.25	0.24	0.02	0.01	0.02
Cr	0.00	0.00	0.00	0.00	0.00	0.00	0.00	0.00	0.00	0.00	0.00
Fe <sup>3+</sup>	0.19	0.22	0.32	0.28	0.31	0.29	0.27	0.31	1.00	1.09	1.26
Fe <sup>2+</sup>	1.34	1.35	1.13	1.31	1.26	1.29	1.31	1.34	0.81	0.60	0.59
Mn	0.02	0.03	0.02	0.02	0.01	0.02	0.01	0.02	0.03	0.00	0.04
Mg	2.83	2.74	2.93	2.79	2.79	2.76	2.78	2.73	3.08	3.23	3.04
Sum C	5.00	5.00	5.00	5.00	5.00	5.00	5.00	5.00	5.00	5.00	5.00
Ca	1.84	1.84	1.85	1.89	1.86	1.87	1.89	1.89	1.66	1.61	1.54
Na	0.16	0.16	0.15	0.11	0.14	0.13	0.11	0.11	0.09	0.08	0.11
Sum B	2.00	2.00	2.00	2.00	2.00	2.00	2.00	2.00	1.75	1.68	1.66
Na	0.42	0.47	0.48	0.55	0.48	0.51	0.53	0.53	0.00	0.00	0.00
K	0.21	0.20	0.18	0.20	0.21	0.22	0.23	0.22	0.05	0.03	0.04
Sum A	0.63	0.67	0.66	0.75	0.69	0.73	0.76	0.75	0.05	0.03	0.04
mg#	0.68	0.67	0.72	0.68	0.69	0.68	0.68	0.67	0.79	0.84	0.84
K <sub>D</sub>	0.93	0.98	0.85	0.97	0.96	0.97	0.97	0.98			
<i>P</i> (Kb)	5.6	6.4	6.3	6.4	6.8	7.1	7.1	6.9			
<i>T</i> (°C)	888	913	923	930	925	936	938	930			

Misho data are from Shahzeidi [2013].



**Table 2.** (continued)

Mineral Rock Sample Location	Amphibole											
	Group 2 xenolith					Host volcanic						
	k-8					v-k-20		v-k-8			v-k	
	Rim 1	Mantle 1	Core	Mantle 2	Rim 2	Core	Core	Core	Core	Core	Core	Core
SiO <sub>2</sub>	41.43	41.47	41.21	41.68	41.25	43/22	43/43	43/31	41.07	41.84	41.64	41.47
TiO <sub>2</sub>	0.83	0.84	0.91	0.88	0.92	1/81	1/88	1/91	2.66	2.23	2.23	2.34
Al <sub>2</sub> O <sub>3</sub>	15.85	16.03	16.61	15.56	15.82	9/12	9/08	9/02	12.02	11.31	10.48	10.91
Cr <sub>2</sub> O <sub>3</sub>	0.05	0.05	0.04	0.08	0.08	0.03	0.02	0.02	0.00	0.10	0.03	0.00
FeO(t)	11.54	11.41	11.57	11.72	11.71	16/98	16/92	16/78	13.70	12.81	18.26	18.01
MnO	0.22	0.17	0.15	0.13	0.12	0/46	0/51	0/52	0.25	0.22	0.51	0.55
MgO	12.64	12.64	12.32	12.64	12.42	11/4	11/23	11/42	12.09	12.57	9.64	9.92
CaO	10.51	10.56	10.71	10.62	10.75	11/12	11/21	11/02	11.57	11.78	11.05	11.36
Na <sub>2</sub> O	2.97	3.02	2.90	2.98	2.92	2/14	2/06	2/01	2.58	2.12	1.99	2.09
K <sub>2</sub> O	0.20	0.24	0.31	0.32	0.57	1/43	1/35	1/32	1.19	1.53	1.70	1.69
Total	96.24	96.43	96.73	96.61	96.56	97.70	97.70	97.34	97.12	96.50	97.51	98.34
Cations calculated on the basis of 23 oxygens												
Si	6.02	6.02	5.97	6.05	6.02	6/46	6/50	6/48	6.14	6.28	6.31	6.24
Al <sup>IV</sup>	1.98	1.98	2.03	1.95	1.98	1/54	1/50	1/52	1.86	1.72	1.69	1.76
Sum T	8.00	8.00	8.00	8.00	8.00	8	8	8	8.00	8.00	8.00	8.00
Al <sup>VI</sup>	0.74	0.76	0.81	0.72	0.74	0/07	0/10	0/07	0.26	0.29	0.18	0.17
Ti	0.09	0.09	0.10	0.10	0.10	0/20	0/21	0/21	0.30	0.25	0.25	0.27
Cr	0.01	0.01	0.00	0.01	0.01	0/01	0/01	0/01	0.00	0.01	0.00	0.00
Fe <sup>3+</sup>	0.91	0.85	0.81	0.82	0.73	0/60	0/53	0/65	0.32	0.21	0.49	0.46
Fe <sup>2+</sup>	0.49	0.53	0.59	0.60	0.70	1/52	1/59	1/45	1.40	1.40	1.82	1.80
Mn	0.03	0.02	0.02	0.02	0.01	0/06	0/06	0/07	0.03	0.03	0.07	0.07
Mg	2.74	2.74	2.66	2.74	2.70	2/54	2/50	2/55	2.69	2.81	2.18	2.23
Sum C	5.00	5.00	5.00	5.00	5.00	5	5	5	5.00	5.00	5.00	5.00
Ca	1.64	1.64	1.66	1.65	1.68	1/78	1/80	1/77	1.85	1.90	1.79	1.83
Na	0.36	0.36	0.34	0.35	0.32	0/22	0/20	0/23	0.15	0.10	0.21	0.17
Sum B	2.00	2.00	2.00	2.00	2.00	2	2	2	2.00	2.00	2.00	2.00
Na	0.47	0.49	0.48	0.49	0.51	0/40	0/39	0/35	0.60	0.51	0.38	0.44
K	0.04	0.04	0.06	0.06	0.11	0/27	0/26	0/25	0.23	0.29	0.33	0.32
Sum A	0.51	0.54	0.54	0.55	0.61	0/67	0/65	0/60	0.83	0.81	0.71	0.76
mg#	0.85	0.84	0.82	0.82	0.79	0/63	0/61	0/64	0.66	0.67	0.54	0.55
K <sub>D</sub>	0.94	0.93	0.97	0.96	0.97	0/28	0/28	0/27				
<i>P</i> (Kb)	9.8	9.9	10.4	9.5	9.8	6.7	6.1	5.9				
<i>T</i> (°C)	964	968	971	960	965	850	846	846				

different from micas of their host volcanic rocks. The biotites from Group 1 hornblendite xenoliths indeed have higher SiO<sub>2</sub>, MgO, CaO, and Al<sub>2</sub>O<sub>3</sub> contents and lower FeO(t), K<sub>2</sub>O, TiO<sub>2</sub>, and Na<sub>2</sub>O contents than micas from their host volcanic rocks (Table 4).

The composition of the biotites in these xenoliths is finally also different from those of Misho diorites [Shahzeidi, 2013]. They indeed display higher TiO<sub>2</sub>, MgO, and Na<sub>2</sub>O and lower Al<sub>2</sub>O<sub>3</sub>, FeO(t), and K<sub>2</sub>O compared to those biotites from Misho diorites.

**Table 3.** Mineral chemical composition of feldspars in hornblendite xenoliths and host volcanic rocks

Mineral Rock Sample Location	Feldspar												
	Group 1 xenolith				Group 2 xenolith				Host volcanic				
	k	k	k-6	k-6	k-8	k-8	k-8	v-k	v-k	v-k	v-k	v-k	v-k-6
Core	Core	Core	Core	Core	Core	Core	Rim 1	Mantle 1	Core 1	Mantle 2	Rim 2	Core	
SiO <sub>2</sub>	60.58	60.37	59.00	59.37	51.51	51.12	51.38	60.83	60.44	58.53	60.21	62.35	71.41
TiO <sub>2</sub>	0.00	0.00	0.01	0.03	0.02	0.03	0.04	0.00	0.04	0.04	0.02	0.02	0.15
Al <sub>2</sub> O <sub>3</sub>	24.56	24.42	25.77	24.68	30.94	30.20	30.88	24.06	25.05	26.39	25.17	23.73	15.13
Cr <sub>2</sub> O <sub>3</sub>	0.02	0.00	0.00	0.01	0.01	0.02	0.02	0.00	0.00	0.00	0.01	0.00	0.01
FeO(t)	0.16	0.18	0.43	0.21	0.31	0.30	0.32	0.19	0.20	0.18	0.42	0.24	1.18
MnO	0.00	0.00	0.02	0.05	0.02	0.03	0.06	0.04	0.04	0.01	0.00	0.03	0.02
MgO	0.00	0.02	0.00	0.01	0.02	0.02	0.01	0.03	0.01	0.00	0.02	0.02	0.21
CaO	6.92	6.88	8.30	7.36	13.87	13.92	13.94	6.04	6.86	8.63	7.15	5.48	1.36
Na <sub>2</sub> O	7.07	7.17	6.25	6.92	3.44	3.35	3.28	7.32	7.18	6.39	6.85	7.61	2.19
K <sub>2</sub> O	0.76	0.73	0.67	0.69	0.12	0.15	0.14	0.89	0.76	0.59	0.81	1.04	5.87
Total	100.07	99.75	100.44	99.32	100.24	99.14	100.07	99.38	100.58	100.76	100.64	100.52	97.53
Cations calculated on the basis of 8 oxygens													
Si	2.42	2.42	2.35	2.39	2.06	2.06	2.05	2.45	2.40	2.32	2.39	2.48	2.93
Al	1.31	1.31	1.37	1.33	1.65	1.62	1.65	1.29	1.33	1.40	1.33	1.26	0.83
Ti	0.00	0.00	0.00	0.00	0.00	0.00	0.00	0.00	0.00	0.00	0.00	0.00	0.01
Fe	0.01	0.01	0.03	0.02	0.02	0.02	0.03	0.02	0.02	0.02	0.03	0.02	0.10
Mn	0.00	0.00	0.00	0.00	0.00	0.00	0.00	0.00	0.00	0.00	0.00	0.00	0.00
Mg	0.00	0.00	0.00	0.00	0.00	0.00	0.00	0.00	0.00	0.00	0.00	0.00	0.02
Zn	0.00	0.00	0.00	0.00	0.00	0.00	0.00	0.00	0.00	0.00	0.00	0.00	0.00
Ca	0.55	0.55	0.66	0.59	1.11	1.12	1.11	0.49	0.55	0.69	0.57	0.44	0.11
Na	1.13	1.15	1.00	1.12	0.55	0.54	0.52	1.15	1.14	1.01	1.09	1.21	0.36
K	0.12	0.12	0.11	0.11	0.02	0.02	0.02	0.14	0.12	0.09	0.13	0.17	0.96
Total	5.55	5.56	5.52	5.56	5.40	5.41	5.39	5.55	5.56	5.53	5.55	5.58	5.32
Or	6.71	6.41	6.01	6.10	1.14	1.43	1.35	8.04	6.70	5.26	7.17	9.11	67.19
Ab	62.61	63.25	56.48	61.30	32.74	32.03	31.57	64.67	63.13	56.54	61.01	66.82	25.04
An	30.68	30.34	37.51	32.61	66.11	66.54	67.08	27.29	30.17	38.21	31.82	24.08	7.77

### 5.2. Whole-rock major and trace element compositions

Major and trace element analyses of hornblendite xenoliths (four samples from Group 1 and three samples from Group 2) are presented in Table 5. In Figure 8a, the samples of the host volcanic rocks plot within the alkaline field (a sample plot within the subalkaline/tholeiitic field) [Cox *et al.*, 1979] while in Figure 8b the host volcanic rocks [Khezerlou *et al.*, 2017], fall within the shoshonite field except for a

sample plotting on the line dividing the shoshonite and calc-alkaline fields. Host volcanic rocks include trachyandesites (samples v-kh-65, v-kh-52 and v-k-20) and basalt trachyandesites (samples v-kh-87, v-kh-93 and k-26), and as mentioned, Group 1 and Group 2 hornblendite xenoliths are located within the trachyandesite field.

Host volcanic rocks (trachyandesites) [Khezerlou *et al.*, 2017] contain lower FeO(t), MgO, TiO<sub>2</sub> and CaO contents and higher SiO<sub>2</sub>, P<sub>2</sub>O<sub>5</sub>, K<sub>2</sub>O, and Na<sub>2</sub>O contents compared to those of Group 1 and Group 2

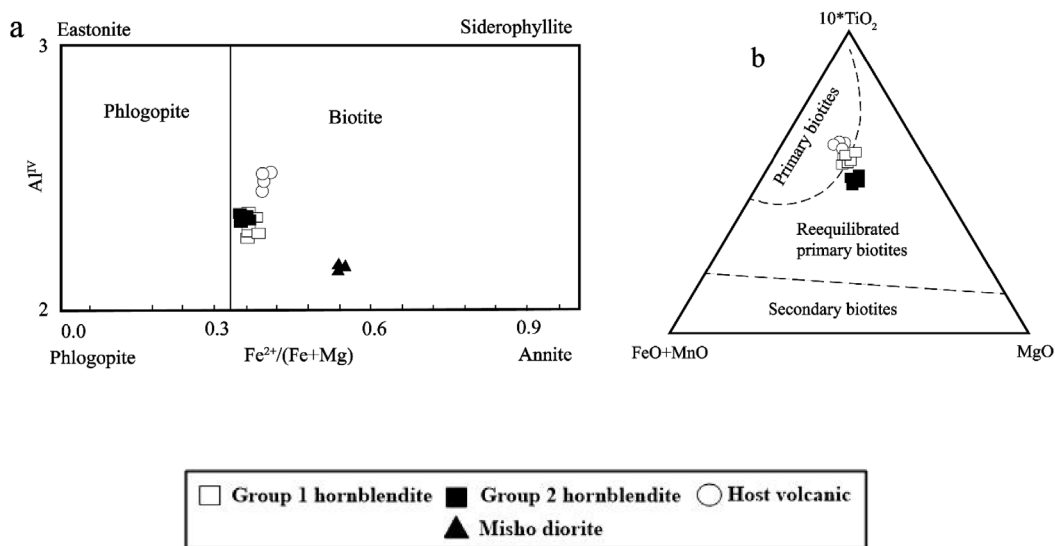


**Figure 7.** (a) Classification of micas [Speer, 1984]. (b) Composition of biotites in the  $10^*TiO_2-FeO-MgO$  diagram [Nachit *et al.*, 2005].

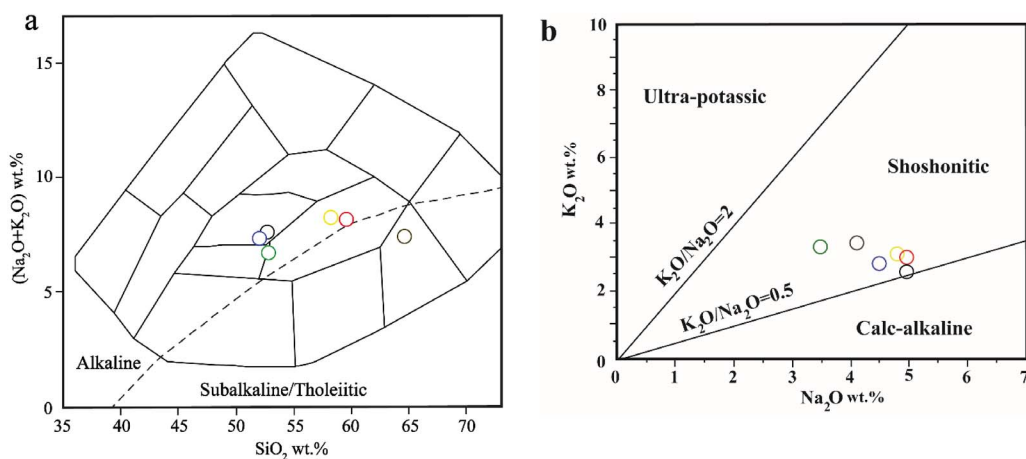


**Figure 8.** Host volcanic rocks. (a) Plotted in the TAS diagram [Cox *et al.*, 1979]. Dashed line separates subalkaline from alkaline rocks. Most of the data plot in the alkaline field. (b) Plotted in the  $Na_2O$  versus  $K_2O$  diagram [after Turner *et al.*, 1996]. The trachyandesites (host volcanics) are from Khezerlou *et al.* [2017]. (The blue, black, and green circles are basalt trachyandesite. The red, yellow, and brown circles are trachyandesite.)

hornblende xenoliths (Table 5). The  $Mg/Mg+Fe^{2+}$  values of Group 1 and Group 2 hornblende xenoliths range from 0.42 to 0.63, and 0.49 to 0.64, respectively.

Group 1 and Group 2 hornblende xenoliths are characterized by enrichment in U, Ba, Pb, Sm, Nd,

Cs, Ti, and K and depletion in Th, Nb, and Zr (Figures 9a, c). The Ti, Ba, K, U, and Th contents in Group 1 hornblende xenoliths are higher than those of Group 2 hornblende xenoliths and host volcanic rocks [Khezerlou *et al.*, 2017] (Figures 9a, c, e). The Pb and Sr contents of host volcanic rocks

**Table 4.** Mineral chemical composition of biotites in hornblendite xenoliths, host volcanic rocks and Misho diorites

Mineral Rock Sample Location	Biotite										
	Group 1 xenolith					Group 2 xenolith					
	k	k-6	k-6	k-6	k-6	k-6	k-8	k-8	k-8	k-8	k-8
Core	Rim 1	Mantle 1	Core	Mantle 2	Rim 2	Rim 1	Mantle 1	Core	Mantle 2	Rim 2	
SiO <sub>2</sub>	37.22	37.47	37.53	38.84	38.69	38.42	37.12	37.05	37.02	37.11	37.06
TiO <sub>2</sub>	3.76	3.50	4.17	3.88	4.07	4.00	3.11	3.02	3.22	3.14	3.04
Al <sub>2</sub> O <sub>3</sub>	14.46	14.29	14.17	14.96	14.27	13.90	14.52	14.61	14.65	14.55	14.64
Cr <sub>2</sub> O <sub>3</sub>	0.01	0.00	0.01	0.02	0.01	0.04	0.07	0.05	0.01	0.02	0.03
FeO(t)	13.71	14.53	14.68	12.97	13.91	14.80	14.13	14.01	14.06	14.21	14.08
MnO	0.13	0.16	0.17	0.10	0.15	0.14	0.66	0.74	0.54	0.62	0.54
MgO	14.87	14.64	14.50	13.80	14.23	13.77	14.63	14.74	14.68	14.55	14.76
CaO	0.06	0.06	0.17	0.27	0.16	0.19	0.12	0.11	0.09	0.14	0.10
Na <sub>2</sub> O	0.36	0.35	0.30	0.18	0.30	0.30	0.49	0.51	0.47	0.45	0.52
K <sub>2</sub> O	8.30	8.87	8.25	7.72	8.27	8.58	8.21	8.15	8.24	8.26	8.22
Total	92.87	93.89	93.95	92.73	94.05	94.12	93.06	92.99	92.98	93.05	92.99
Cations calculated on the basis of 22 oxygens											
Si	5.64	5.66	5.65	5.82	5.77	5.77	5.65	5.64	5.63	5.65	5.64
Al <sup>IV</sup>	2.36	2.34	2.35	2.18	2.23	2.23	2.35	2.36	2.37	2.35	2.36
Al <sup>VI</sup>	0.22	0.20	0.16	0.46	0.28	0.23	0.25	0.26	0.25	0.25	0.26
Ti	0.43	0.40	0.47	0.44	0.46	0.45	0.36	0.35	0.37	0.36	0.35
Fe <sup>2+</sup>	1.74	1.83	1.85	1.62	1.73	1.86	1.80	1.78	1.79	1.80	1.79
Mn	0.02	0.02	0.02	0.01	0.02	0.02	0.09	0.10	0.07	0.08	0.07
Mg	3.36	3.30	3.25	3.08	3.16	3.08	3.32	3.34	3.33	3.30	3.35
Ca	0.01	0.01	0.03	0.04	0.02	0.03	0.02	0.02	0.01	0.02	0.02
Na	0.11	0.10	0.09	0.05	0.09	0.09	0.14	0.15	0.14	0.13	0.15
K	1.60	1.71	1.58	1.47	1.57	1.64	1.59	1.58	1.60	1.60	1.59
Total	15.48	15.57	15.45	15.18	15.34	15.40	15.57	15.58	15.56	15.54	15.58
#Mg	0.66	0.64	0.64	0.65	0.65	0.62	0.64	0.65	0.65	0.64	0.65

[Khezerlou *et al.*, 2017], on the other hand, are higher than those of hornblendite xenoliths. Although these xenoliths have a cumulate nature and may have lost some of their interstitial residual melt, similarly to their host volcanic rocks [Khezerlou *et al.*, 2017], they show an enrichment in LREE compared to HREE (Figures 9b, d, f). HREE and MREE contents in Group 1 hornblendite xenoliths are higher than that in Group 2 hornblendite xenoliths. Also, LREE content in Group 1 hornblendite xenoliths is higher than that in Group 2 hornblendite xenoliths and lower than that of host volcanic rocks [Khezerlou *et al.*, 2017]. Group 1 hornblendite xenoliths,

similarly to their host volcanic rocks, are characterized by a negative Eu anomaly while Group 2 hornblendite xenoliths display a positive Eu anomaly.

### 5.3. Whole-rock Sr–Nd isotopes

The <sup>86</sup>Sr/<sup>87</sup>Sr and <sup>143</sup>Nd/<sup>144</sup>Nd isotopic ratios were used to investigate and determine the origin of the investigated hornblendite xenoliths. The analyses and the sampling locations are presented in Table 6 and Figure 10, respectively. The results show that the <sup>86</sup>Sr/<sup>87</sup>Sr ratio in Group 1 and Group 2 xenoliths are 0.706291 and 0.704685, respectively,

**Table 4.** (continued)

Mineral Rock Sample Location	Biotite						
	Host volcanic				Misho diorite		
	v-k-6		v-k-20		A2-39-3-2		
	Core	Core	Core	Core	Core	Core	Core
SiO <sub>2</sub>	36.44	36.39	36.28	36.22	37.40	37.30	37.00
TiO <sub>2</sub>	5.04	5.22	5.02	5.13	2.90	2.06	2.25
Al <sub>2</sub> O <sub>3</sub>	13.62	13.78	13.85	13.92	16.10	17.30	17.20
Cr <sub>2</sub> O <sub>3</sub>	0.00	0.00	0.00	0.00	0.02	0.00	0.00
FeO	15.62	16.17	16.14	16.08	21.20	21.90	21.40
MnO	0.25	0.25	0.22	0.24	0.24	0.21	0.19
MgO	13.89	13.48	13.54	13.65	8.80	8.91	8.80
CaO	0.07	0.04	0.12	0.14	0.26	0.13	0.13
Na <sub>2</sub> O	0.62	0.59	0.64	0.69	0.06	0.05	0.08
K <sub>2</sub> O	9.31	9.27	9.16	9.11	8.49	9.11	9.02
Total	94.86	95.20	94.97	95.18	95.47	96.97	96.07
	Cations calculated on the basis of 22 oxygens						
Si	5.52	5.51	5.50	5.48	5.96	5.87	5.87
Al <sup>IV</sup>	2.43	2.46	2.48	2.48	2.04	2.13	2.13
Al <sup>VI</sup>	0.00	0.00	0.00	0.00	0.97	1.08	1.09
Ti	0.57	0.59	0.57	0.58	0.35	0.24	0.27
Fe <sup>2+</sup>	1.98	2.05	2.05	2.03	2.82	2.88	2.83
Mn	0.03	0.03	0.03	0.03	0.03	0.03	0.03
Mg	3.14	3.04	3.06	3.08	2.09	2.09	2.08
Ca	0.01	0.01	0.02	0.02	0.04	0.02	0.02
Na	0.18	0.17	0.19	0.20	0.02	0.01	0.03
K	1.80	1.79	1.77	1.76	1.72	1.83	1.83
Total	15.67	15.64	15.67	15.67	16.04	16.18	16.18
#Mg	0.61	0.60	0.60	0.60	0.43	0.42	0.42

Misho data are from Shahzeidi [2013].

while the <sup>143</sup>Nd/<sup>144</sup>Nd ratio is 0.512580 and 0.512736, respectively. Samples from Group 1 xenoliths plot within EMI and EMII endmembers while those from Group 2 fall within EMII and HIMU fields. To validate the results, some host volcanic rocks and pyroxenite xenoliths [Khezerlou *et al.*, 2017] from the study area and some Misho diorites [Shahzeidi, 2013] were used (Table 6). As illustrated in Figure 10, the host volcanic rocks fall between EMII and upper crust fields (closer to the upper crust). On the other hand, Group 2 pyroxenite xenolith samples fall within EMI and EMII fields while samples from Misho diorite plot far from

xenoliths and host volcanic rocks and closer to EMI endmember.

#### 5.4. Thermobarometry

Since plagioclase in the hornblende xenoliths occurs as the intercumulus phase and therefore formed after cumulus amphibole, the plagioclase–amphibole pairs in these samples cannot be used for thermobarometry. Therefore, only amphibole was used for this purpose. According to Putirka [2016], if  $K_D(\text{Fe–Mg})^{\text{amph–liq}}$  is within  $0.28 \pm 0.11$ , then we may



**Table 5.** Whole-rock major and trace element data for xenoliths and volcanic rocks

Rock Sample	Group 1 xenolith				Group 2 xenolith		
	K	K-6	Kh-52	K-11	K-8	Kh-12	K-21
SiO <sub>2</sub>	43.86	44.20	47.86	48.32	42.52	45.77	44.33
TiO <sub>2</sub>	1.85	1.83	2.21	1.68	1.38	1.49	2.00
Al <sub>2</sub> O <sub>3</sub>	12.39	12.34	15.10	16.26	15.33	15.50	18.29
Fe <sub>2</sub> O <sub>3</sub> (t)	12.62	12.26	14.31	11.67	12.61	12.00	12.24
FeO	7.13	6.93	7.54	6.16	7.32	6.54	6.93
Fe <sub>2</sub> O <sub>3</sub>	4.56	4.44	5.69	4.65	4.30	4.55	4.43
MnO	0.16	0.16	0.20	0.21	0.16	0.16	0.16
MgO	12.11	11.71	5.42	7.29	13.03	7.69	6.66
CaO	10.40	10.33	8.44	10.28	10.42	9.97	10.19
Na <sub>2</sub> O	2.25	2.28	3.24	3.73	2.49	2.87	2.72
K <sub>2</sub> O	1.76	1.85	1.57	1.16	0.80	1.40	1.22
P <sub>2</sub> O <sub>5</sub>	0.30	0.29	0.30	0.25	0.31	0.16	0.18
LOI	1.12	1.21	2.15	0.78	1.17	2.06	1.07
Total	98.82	98.48	100.80	101.61	100.22	99.08	99.07
Sr	282	300	434	568	303	312	494
Ba	356	361	541	592	127	137	261
V	383	380	308	299	242	263	267
Cr	95	84	275	331	342	310	123
Co	63	62	55	42	78	53	50
Ni	138	136	186	62	349	93	78
Y	27	26	32	40	11	21	14
Zr	57	57	81	58	28	47	54
Nb	5.9	6.0	24.5	9.7	7.9	7.2	11.1
Mo	0.5	0.3	0.9	0.5	0.3	0.7	1.0
La	12.5	10.4	15.4	17.6	7.8	6.4	6.4
Ce	34.8	27.4	39.1	38.5	19.0	16.5	16.3
Pr	5.0	4.1	4.1	4.6	2.5	2.1	1.7
Nd	24.5	19.9	16.7	19.7	10.8	10.2	7.5
Sm	6.4	5.1	3.7	4.6	2.2	2.7	1.6
Eu	1.8	1.4	1.2	1.4	0.8	1.0	0.7
Gd	6.7	5.1	4.0	4.8	2.0	3.0	1.6
Tb	0.9	0.7	0.6	0.7	0.3	0.5	0.2
Dy	4.9	3.8	3.8	4.5	1.5	2.9	1.3
Ho	0.9	0.7	0.8	1.0	0.3	0.6	0.3
Er	2.3	1.8	2.1	2.6	0.7	1.6	0.7
Yb	1.7	1.3	1.7	2.2	0.5	1.3	0.5
Lu	0.2	0.2	0.2	0.3	0.1	0.2	0.1

(continued on next page)

**Table 5.** (continued)

Rock Sample	Group 1 xenolith				Group 2 xenolith		
	K	K-6	Kh-52	K-11	K-8	Kh-12	K-21
Hf	2.1	2.2	2.1	1.7	0.7	1.5	1.3
W	19.3	15.9	31.3	38.3	19.9	32.3	28.1
Th	0.6	0.7	1.3	0.7	0.1	0.5	0.3
U	0.5	0.6	0.9	0.4	0.2	0.4	0.4
Cu	22.0	19.6	189.9	12.0	3.6	46.3	85.2
Zn	95.8	82.1	137.5	87.8	55.6	90.9	76.8
Ga	15.1	12.6	16.7	16.4	8.7	15.6	16.1
Rb	46.2	28.1	31.3	6.5	3.8	17.2	8.9
Cs	10.5	15.7	1.6	0.7	0.4	4.2	1.5
Ta	0.3	0.3	1.2	0.4	0.3	0.5	0.6
Pb	5.3	5.1	8.2	9.7	2.2	5.6	4.1
Ba/Nb	60	60	22	61	16	19	23
Ba/Ta	1090	1409	446	1367	417	296	432
Nb/La	0.5	0.6	1.6	0.6	1.0	1.1	1.7
(Ce/Yb)N	5.4	5.5	5.9	4.5	9.2	3.2	8.3
(Dy/Yb)N	1.9	1.9	1.4	1.3	1.9	1.5	1.7
Ce/Pb	6.6	5.3	4.7	4.0	8.7	2.9	4.0
#Mg	0.63	0.63	0.42	0.54	0.64	0.54	0.49

Major elements in wt%, trace elements and REE in ppm.

**Table 6.** Sr and Nd isotopic (whole rock) composition of xenoliths, a volcanic rock from NW Marand area and Misho diorites

Rock Sample	Group 1 xenolith k-11	Group 2 xenolith kh-12	Host volcanic v-kh-52	Pyroxenitic xenoliths			Misho diorites	
				kh-62	kh-64	kh14	A2-43-1	A2-11-1
$^{87}\text{Sr}/^{86}\text{Sr}$	0.706291	0.704685	0.709545	0.707026	0.706825	0.70642	0.704861	0.705815
$2\sigma$	0.000003	0.000002	0.000002	0.000003	0.000003	0.000002	0.000013	0.000011
$^{143}\text{Nd}/^{144}\text{Nd}$	0.512580	0.512736	0.512561	0.512525	0.512482	0.512501	0.512155	0.512010
$2\sigma$	0.000003	0.000002	0.000002	0.000003	0.000002	0.000002	0.000012	0.000011
$\epsilon\text{Nd}$	-1.06	1.96	-1.27	-1.98	-2.81	-2.45	-0.61	1.2

Host volcanic rock and pyroxenitic xenolith data are from Khezerlou *et al.* [2017] and Misho data are from Shahzeidi [2013].

assume that the amphibole is in equilibrium with the melt. The  $K_D$  from the investigated hornblende xenoliths is not equal to  $0.28 \pm 0.11$  (Table 2). As a result, estimate may be obtained from Hammarstrom and Zen [1968] method ( $P = -3.92 + 5.03 \text{Al}_{\text{total}}$ ). This method independent of the temperature is solely based on the  $\text{Al}_{\text{total}}$  content of the amphibole. The

pressure of formation of amphibole minerals from Group 1 and Group 2 hornblende xenoliths using that equation ranges from 5.5 to 7 kbar and 9.5 to 10.5 kbar, respectively (Table 2). Also, according to the diagram of  $\text{Al}_{\text{total}}$  versus  $\text{Fe}/\text{Fe}+\text{Mg}$ , the formation pressure of amphiboles of Group 1 and Group 2 hornblende xenoliths has been estimated to be

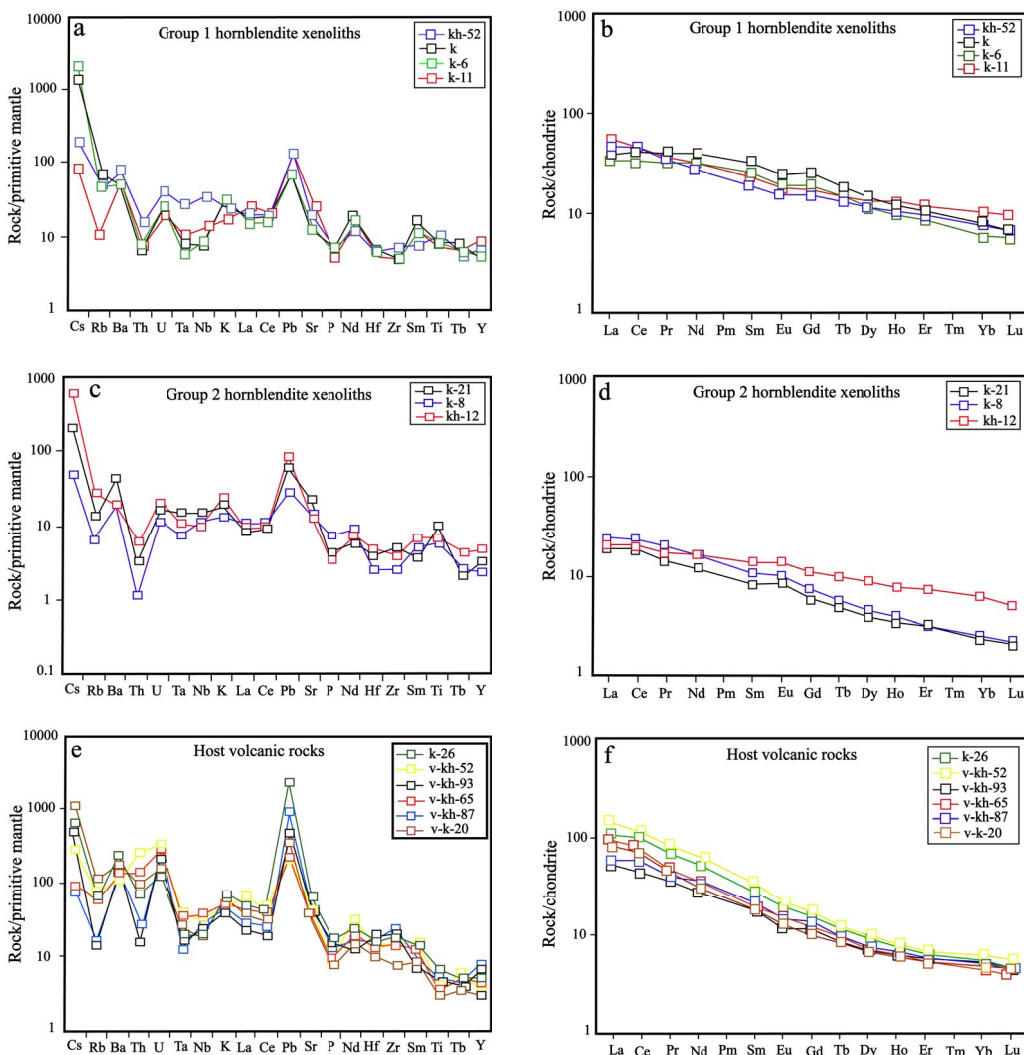


**Figure 9.** (a, c, e) Primitive mantle normalized spidergrams and (b, d, f) chondrite normalized REE patterns of hornblende xenoliths. Chondrite and primitive mantle values are from Boynton [1984] and Sun and McDonough [1989], respectively. Host volcanics data are from Khezerlou *et al.* [2017].

**Table 7.** Modal compositions of xenoliths estimated by using the whole rock and constituent minerals' major element compositions and a mixing model based on least squares method

Rock	Sample	Clinopyroxene	Amphibole	Plagioclase	Biotite	Total
Group 1 xenolith	k	1	81	8	10	100
	k-6		84	6.5	9.5	100
Group 2 xenolith	k-8		94	3	3	100

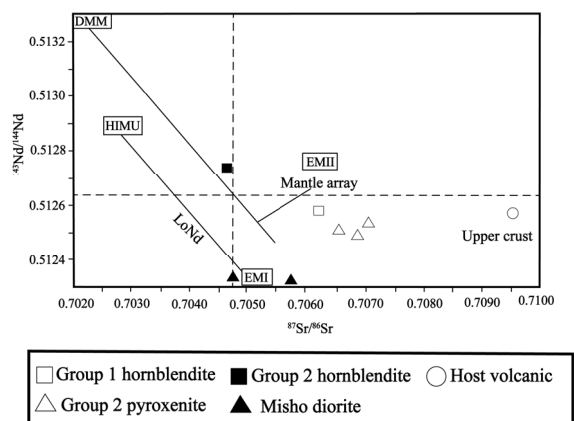


**Figure 10.**  $^{143}\text{Nd}/^{144}\text{Nd}$  versus  $^{87}\text{Sr}/^{86}\text{Sr}$  diagram for the whole rock of investigated samples. The fields for DMM, HIMU, EMI, EMII and upper crust are from Zindler and Hart [1986]. LoNd array is from Hart et al. [1986]. Misho data are from Shahzeidi [2013] and pyroxenite xenoliths and host volcanic data are from Khezerlou et al. [2017].

more than 5.5 kbar (Figure 11). Unlike xenoliths, the  $K_D$  of the investigated host volcanic rock (0.27–0.28) fall within the range  $0.28 \pm 0.11$ , the chemical composition of their amphibole and whole rock is therefore suitable to be used for barometry, as stressed above. The estimated formation pressures for amphiboles of host volcanic rock (v-k-20 sample) according to the Equation (7c)  $\{P(\text{kbar}) = -45.5 - 46.3[\ln(D_{\text{Al}}^{\text{anhyd}})] - 41.1[\ln(X_{\text{Al}_2\text{O}_3}^{\text{anhyd}})] + 439[X_{\text{P}_2\text{O}_5}^{\text{anhyd}}] + 26.6[\text{Al}^{\text{amph}}] + 22.5[\text{K}^{\text{amph}}] + 5.23[\ln(D_{\text{Na}}^{\text{anhyd}})]\}$  proposed by Putirka [2016] are 6–6.7 kbars.

The formation temperatures of amphibole minerals from Group 1 and Group 2 hornblende xenoliths and host volcanic rock (v-k-20 sample) estimated according to the Equation (5)  $\{T \text{ } ^\circ\text{C} = 1781 - 132.74[\text{Si}^{\text{amph}}] + 116.6[\text{Ti}^{\text{amph}}] - 69.41[\text{Fe}_t^{\text{amph}}] + 101.62[\text{Na}^{\text{amph}}]\}$  proposed by Putirka [2016] range from 890 to 940  $^\circ\text{C}$ , 960 to 970  $^\circ\text{C}$ , and 846 to 850  $^\circ\text{C}$ , respectively (Table 2).

The crystallization depth of amphibole from Group 1 and Group 2 hornblende xenoliths and host volcanic rock was therefore estimated to be 17–20 km, 30–35 km, and 18–20 km, respectively. Since the crustal thickness from the study area has been estimated to range from 40 to 45 km [Dehghani and Makris, 1984], amphiboles from Group 1

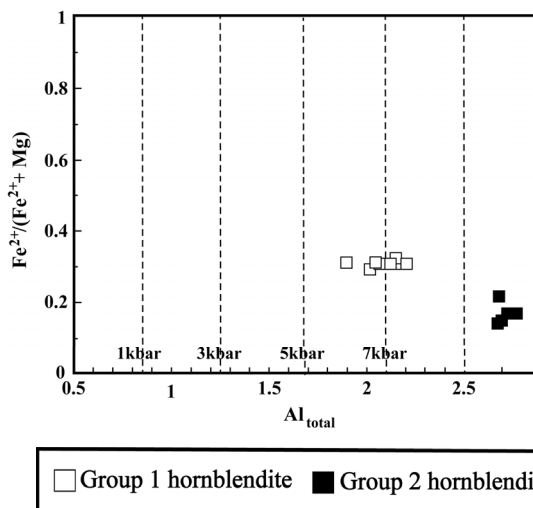


**Figure 11.** Plot of  $\text{Al}_{\text{total}}$  versus  $\text{Fe}^{2+}/(\text{Fe}^{2+} + \text{Mg})$  for amphiboles from the hornblende xenoliths [Hammarstrom and Zen, 1968].

hornblende xenoliths and host volcanic rocks (trachyandesite) might have been formed within this crust while those of Group 2 hornblende xenoliths have been also formed within the crust but closer to the crust–mantle boundary.

### 5.5. Oxygen fugacity

The differences observed in the  $\text{Fe}^{3+}$  content of clinopyroxene from the investigated samples could be ascribed to different oxidation and oxygen fugacity states of the magma they crystallized from [Canil and Fedortchouck, 2000, Aydin, 2008]. The Na, Al(IV), and  $\text{Fe}^{3+}$  contents of the clinopyroxenes from host volcanic rocks are higher than those of the clinopyroxene from Group 1 hornblende xenoliths, suggesting that they formed at higher oxidation conditions [Schweitzer et al., 1979]. The location of samples in Figure 4d supports such an inference. It can also be seen in this figure (Figure 4d) that clinopyroxenes from the host volcanic rock are formed in conditions of high oxidation compared to the pyroxenite xenoliths of the study area [Khezerlou et al., 2017] and Misho diorites [Shahzeidi, 2013]. Also, the location of samples in Figure 5d indicates crystallization of amphibole from Group 1 and Group 2 hornblende xenoliths and host volcanic rock under high oxidation conditions.

As can be seen in Figure 5d, the amount of  $\text{Fe}^{2+}$  in amphiboles from Group 2 hornblendite xenoliths is lower than those of amphiboles from Group 1 hornblendite xenoliths and host volcanic rocks, indicating that they formed at higher oxidation conditions. Assuming that the formation pressure of amphiboles is directly related to oxygen fugacity [Stein and Dietl, 2001], it is likely that amphiboles from Group 2 were formed at higher pressures than those from Group 1 and host volcanic rocks, a result consistent with the barometric estimates.

### 5.6. *Characteristics of magma sources*

The changes in composition from core to rim of amphibole from Group 1 are normally associated with a temperature increase. These compositional changes in amphibole probably suggest the injection of pulses of magma.

The amphiboles and biotites from Group 2 hornblendite xenoliths do not show clear zoning (Tables 2 and 4, respectively), suggesting their gradual crystallization and equilibration with the melt during the crystallization process. On the other hand the biotites from Group 1 hornblendite xenoliths are zoned with a decrease of  $\text{Al}_2\text{O}_3$ ,  $\text{SiO}_2$ , and  $\text{CaO}$  associated to an increase of  $\text{MgO}$ ,  $\text{FeO}$ , and  $\text{K}_2\text{O}$  from core to rim (Table 4). It seems that during the crystallization of biotites, plagioclases also crystallized and as Si, Ca, and Al are preferably incorporated within the structure of plagioclase, that process could explain the lower concentrations of those elements in the rim of biotite crystals. As mentioned in the petrography section, plagioclases from Group 1 hornblendite xenoliths are mainly intercumulus and it seems therefore that plagioclases and biotites were not accumulated simultaneously. The normal zoning observed in the plagioclase phenocrysts from the host volcanic rocks (Table 3) indicates a temperature decrease of the residual melt as crystallization proceeded.

The petrographic study (for example the presence of some coarse-grained amphiboles and biotites and euhedral amphiboles) confirms the cumulus texture of the xenoliths. Positive anomalies of U, Ba, Ti, and K in hornblendite xenoliths are probably related to the accumulation process of amphibole and biotite (Figures 9a, c).

Biotites from hornblendite xenoliths and host volcanic rocks display very low Al(VI) content, which

is sometimes totally absent (Table 4), suggesting a magmatic origin [Nachit *et al.*, 2005]. The position of xenoliths and host volcanic rocks in the ternary diagram  $\text{MgO}$ ,  $\text{FeO}+\text{MnO}$ , and  $10\text{TiO}_2$  also indicates a magmatic origin. Since the amphiboles and biotites in the hornblendite xenoliths and host volcanic rocks are of igneous type, due to the fact that amphibole and biotite are hydrous minerals and they are formed in hydrous conditions, it may be inferred that their parental magmas contained relatively high amounts of water [Otten, 1984].

The anorthite content of plagioclases typically gives constraint on the water content of their parental magma [e.g. Sisson and Grove, 1993]. According to Sisson and Grove [1993], the distribution coefficient of calcium–sodium between plagioclase and melt is sensitive to  $P_{\text{H}_2\text{O}}$ , and varies from 1 to 5.5 under water-free and water-saturated conditions, respectively. As a result, the high content of anorthite is related to the high water pressure in the melt. Thus, the plagioclases from the Group 2 hornblendite xenoliths might have crystallized from a magma with a higher  $\text{H}_2\text{O}$  content than that of the magma from which the Group 1 hornblendite xenoliths and host volcanic rocks crystallized (Figure 6). However, the anorthite content of plagioclase may also change with the degree of crystal fractionation. The difference in isotope ratios suggests that the xenolith groups and the host volcanic rock were formed from different parental melts.

According to Anderson and Smith [1995] the  $\text{Mg}\#$  of amphibole is strongly dependent on the degree of crystallization. Therefore, the difference in the  $\text{Mg}\#$  of amphiboles in Group 1 (0.67–0.72) and Group 2 (0.79–0.85) xenoliths and host magma samples (0.54–0.67) could suggest different degrees of crystallization of their respective parental melts. Yet, the high  $\text{Mg}\#$  of amphibole is also related to high oxygen fugacity. Therefore, the high  $\text{Mg}\#$  of amphiboles in Group 2 could also point to a higher oxygen fugacity compared to Group 1 and host volcanic rocks, as suggested by the position of the samples in Figure 5d.

The Ti content in clinopyroxene may give indication on the degree of depletion of the magma mantle source [Pearce and Norry, 1979]. In this regard, the difference in Ti concentration of clinopyroxene from Group 1 hornblendite xenoliths (0.19–0.21) and host volcanic rocks (1.21–1.28) may be attributed to variable depletion and degree of partial melting of their



respective mantle sources. It indicates a higher enriched source for the parental magma of host volcanic rocks compared to that of the Group 1 hornblende xenoliths. This is also confirmed by the  $^{86}\text{Sr}/^{87}\text{Sr}$  isotopic ratios (Figure 10).

The lower LREE, Pb, Th, Ba and U contents and low  $^{86}\text{Sr}/^{87}\text{Sr}$  ratio in Group 2 xenoliths compared to those of Group 1 indicate a more depleted mantle source for this group (Table 6). Besides, the difference in  $^{86}\text{Sr}/^{87}\text{Sr}$  and  $^{143}\text{Nd}/^{144}\text{Nd}$  values of Group 1 and Group 2 xenoliths and host volcanic rocks suggests also a difference in composition of their respective mantle sources [Zhang *et al.*, 2006].

Positive Pb anomaly in xenoliths and host volcanic rocks indicates either the influence of mantle wedge metasomatism through fluids from subducting oceanic plate for the sources of magmas or contamination of magmas by the crustal lithosphere [Atherton and Ghni, 2002]. Positive Ba, La, Cs, K, and U anomalies associated with negative Nb and Ta anomalies may be explained by magma contamination by crustal materials [Hofmann, 1997].

In all the investigated xenoliths, a negative Th anomaly is observed (Figures 9a, c). This element has a low mobility in arc settings [Pearce and Peate, 1995] due to its very low solubility in subduction zone fluids. The observed negative Th anomaly is therefore probably due to the effect of fluids released from a subducted oceanic plate. Similarly to host volcanic rocks [Khezerlou *et al.*, 2017], negative Nb and Ta anomalies are also observed in hornblende xenoliths and probably also reflect a subduction-related magmatism (Figures 9a, c, e) [Saunders *et al.*, 1980, Kuster and Harms, 1998]. According to Ionov and Hofmann [1995], amphibole is a very suitable mineral for storing Nb and Ta in the upper mantle and can impart negative anomalies of Nb and Ta on subduction zone magmas. Due to the high thickness of the continental crust in the study area (40–45 km), contamination of magma by crustal materials can also be effective.

As shown in Table 5, the  $(\text{Ce}/\text{Pb})_{\text{N}}$  ratio in the investigated xenoliths, similarly to that of host volcanic rocks [Khezerlou *et al.*, 2017], is lower than 18 while for MORB and oceanic arc environments it is 47 and 27, respectively [Hofmann *et al.*, 1986]. This low ratio in xenoliths and host volcanic rocks probably implies the presence of crustal materials in their parental magma sources [Yang *et al.*, 2005]. High

abundance of LREE and LILE in hornblende xenoliths agrees with the involvement of a metasomatized upper mantle in their genesis. Previous studies on volcanic rocks [Ahmadzadeh *et al.*, 2010] and pyroxenite xenoliths [Khezerlou *et al.*, 2017] from the study area also evidenced a metasomatized mantle source leading to the enriched characteristics of the parental magmas.

The higher abundances of U, Ba, and K in Group 1 xenoliths compared to those of Group 2 could be explained by the higher biotite modal content of the former as these three elements are preferentially incorporated by biotite than by amphibole. In addition, the higher MREE content characterizing most of the Group 1 hornblende xenoliths compared to those of Group 2 and host volcanic rocks could be related to their higher amphibole modal content, which is also in agreement with the higher Ti content of Group 1 hornblende xenoliths.

The negative Eu anomaly in Group 1 hornblende xenoliths, similar to that in host volcanic rocks [Khezerlou *et al.*, 2017], evidence early fractionation of Ca-plagioclase from the parental magma during its journey in the crust [Willson, 1989, Martin, 1999, Wu *et al.*, 2003]. On the other hand, the positive Eu anomaly in Group 2 hornblende xenoliths is associated with high plagioclase (labradorite) modal content.

As shown in Figure 8, the amount of  $\text{SiO}_2$ ,  $\text{K}_2\text{O}$ , and  $\text{Na}_2\text{O}$  in the xenoliths is lower than that of the host volcanic rocks, and this is associated with a higher abundance of LREE (including: La, Ce, Pr and Nd) in the host lava relative to xenoliths. The higher contents of all these elements in the host lava could be related to the contamination of its parental melt by crustal material. The  $^{86}\text{Sr}/^{87}\text{Sr}$  ratio of the host volcanic rock (0.709545) is higher than those of the xenoliths (Group 1 = 0.706291 and Group 2 = 0.704685), but its  $^{143}\text{Nd}/^{144}\text{Nd}$  ratio does not differ much from that of the xenoliths. As magma contamination by crustal materials increases the  $^{86}\text{Sr}/^{87}\text{Sr}$  ratio and decreases the  $^{143}\text{Nd}/^{144}\text{Nd}$  ratio, it therefore seems that magma contamination by crustal material cannot explain the high  $^{86}\text{Sr}/^{87}\text{Sr}$  ratio of host volcanic rocks. It is likely that the main cause of the differences observed between xenoliths and host volcanic rocks is related to a more enriched mantle source for the parental magma of host volcanic rocks. This explanation could also apply to the difference in the content of LREE of Group 1 and Group 2

xenoliths. The higher LREE content and  $^{86}\text{Sr}/^{87}\text{Sr}$  ratio of Group 1 xenoliths compared to those of Group 2 xenoliths could be indeed related to a more enriched mantle source for the parental magma of the Group 1 xenoliths.

The high HREE content of Group 1 xenoliths compared to that of Group 2 xenoliths is probably due to the presence of clinopyroxene in Group 1 samples, because these elements are preferentially incorporated in clinopyroxene. On the other hand the low amounts of MREE of Group 2 could be explained by a lower modal content of amphibole in Group 2 compared to Group 1 xenoliths [Gertisser and Keller, 2000].

The Yb content in the investigated xenoliths is lower than 4 ppm (on average 1.16). Thus, it could be considered that these xenoliths did not crystallize from primary magma [Irving and Frey, 1978]: which suggests in turn that the parental magmas of xenoliths probably underwent fractional crystallization processes of garnet and clinopyroxene prior to xenolith crystallization. The lack of garnet (Group 1 and 2) and paucity (Group 1) or lack of clinopyroxene (Group 2) in the investigated xenoliths seem to confirm this.

### 5.7. Generation of the xenoliths

Many studies have related intra-continental alkaline rocks to the presence of mantle plumes [Hofmann and White, 1982, Willson, 1989]. Magmatism associated with mantle plumes is characterized by a very high production of melts [Willson, 1989], which contrasts with the limited outcrops of alkaline rocks in the investigated area. Usually the shape of mantle plumes are symmetric [Willson, 1989], but Khezerlou *et al.* [2017] have shown that the volcanic shape of the investigated area and of the Uromieh Dokhtar belt is not symmetrical being oriented northwest–southeast and almost parallel to the Zagros orogenic belt. Altogether, geochemical features of host volcanic rocks and the two groups of xenoliths such as Nb and Ta depletion are inconsistent with magmas originated from the activity of a mantle plume.

The two groups of investigated hornblendite xenoliths and host volcanic rocks display distinct LILE and LREE enrichment, Ta and Nb depletion and high Ba/Ta and Ba/Nb ratios, which are among the characteristics of subduction-derived magmatic

rocks. Previous studies attributed the magmatism of Uromieh-Dokhtar zone to the subduction of the Neotethys underneath the Iranian continental crust [e.g. Nicolas, 1989, Hassanzadeh, 1993, Ghasemi and Talbot, 2006] probably during Middle Cretaceous [Ghasemi and Talbot, 2006]. This Neotethys ocean closed during the Upper Cretaceous [Nicolas, 1989]. The subduction of the Neotethys led to the metasomatism of the mantle wedge located above the subducting plate.

The geochemical features of the investigated xenoliths as well as their  $^{86}\text{Sr}/^{87}\text{Sr}$  and  $^{143}\text{Nd}/^{144}\text{Nd}$  ratios, are in agreement with the occurrence of such type of metasomatism in the northern part of Uromieh Dokhtar magmatic belt. As the subduction continued, the subducted oceanic plate was broken (slab break-off). The uplift of hot asthenosphere through the resulting slab window led to the melting of the metasomatized lithospheric mantle [Keskin, 2003, Jahangiri, 2007, Kheirkhah *et al.*, 2009]. Considering the relative age of the host volcanic rocks (Plio-Quaternary), it appears that the magmatism of the study area occurred at later stages following the collision. Post-collision tension processes activated faults in the study area. As mentioned in the geological setting section, the studied alkaline rocks are commonly located along the main faults. Therefore it seems that the movement of the main faults (especially North Tabriz Fault, North Misho and Tasuj faults) has provided a path for the lavas carrying the investigated xenoliths to penetrate the continental crust. As a result, magmas were trapped during their ascent to the surface at different levels of the crust. Subsequent to their crystallization, amphiboles and micas accumulated on the floor of some temporary deep seated magma chambers. Xenoliths eventually reached the ground surface through the later magmatic activity.

## 6. Conclusions

Field surveys performed in the present work show that alkaline volcanic rocks from the study area are Plio-Quaternary in age. The results of petrographic studies evidence cumulus processes in these magmatic xenoliths. There are differences in REE content and  $^{86}\text{Sr}/^{87}\text{Sr}$  and  $^{143}\text{Nd}/^{144}\text{Nd}$  ratios as well as in the chemical composition of their constituent minerals between Group 1 and Group 2

hornblendite xenoliths. This indicates that their respective parental magmas likely were derived from different mantle sources.

The high LREE and LILE contents of both groups of hornblendite xenoliths imply the presence of metasomatized enriched mantle sources beneath the study area. It is likely that as the parental magma ascends upwards some minerals, including olivine and clinopyroxene, separated from the magma after crystallization. The resulting magmas were emplaced at different depths within the crust. An explanation for this observation is that micas and amphiboles from the xenoliths accumulated on the floor of magmatic reservoirs after crystallization in the crust and reached the ground surface through a later magmatic activity. Thermometry results using amphiboles show that crystallization depth of Group 1 and Group 2 xenoliths range from 17 to 20 km and from 30 to 35 km within the crust, respectively.

The difference in isotope ratios and the composition of the clinopyroxenes suggest that the hornblendite xenoliths and the pyroxenite xenoliths from the study area were formed from different parental melts.

Finally by comparing  $^{86}\text{Sr}/^{87}\text{Sr}$  and  $^{143}\text{Nd}/^{144}\text{Nd}$  ratios and chemical composition of minerals from the investigated xenoliths and Misho diorites, we may conclude that hornblendite xenoliths are not linked to the Misho diorites.

## Acknowledgments

This research is a part of the Ph.D. dissertation of the first author which he accomplished with the support of the Vice Chancellor for Research and High Education of Tabriz University (Iran). Hereby, we thank authorities of Tabriz University for their help and cooperation. The authors also thank the Laboratoires Géosciences Environnement Toulouse and Géosciences Marines (Brest) of France that allowed us to perform the various mineralogical and geochemical analyses.

## References

- Aghazadeh, M., Prelević, D., Badrzadeh, Z., Braschi, E., Bogaard, P., and Conticelli, S. (2015). Geochemistry Sr–Nd–Pb isotopes and geochronology of amphibole and mica-bearing lamprophyres in north-western Iran: implications for mantle wedge heterogeneity in a paleo-subduction zone. *Lithos*, 216–217, 352–369.
- Ahmazadeh, G., Jahangiri, A., Lentz, D., and Mojtahe, M. (2010). Petrogenesis of Plio-Quaternary post-collisional ultrapotassic volcanism in NW of Marand, NW Iran. *J. Asian Earth Sci.*, 39, 37–50.
- Alavi, M. (2004). Regional stratigraphy of the Zagros folded-thrust belt of Iran and its proforeland evolution. *Am. J. Sci.*, 304, 1–20.
- Anderson, J. L. and Smith, D. R. (1995). The effects of temperature and  $f\text{O}_2$  on the Al-in-hornblende barometer. *Am. Mineral.*, 80, 549–559.
- Atherton, M. P. and Ghni, A. A. (2002). Slab break-off: a model for Caledonian, late granite syn-collisional magmatism in the orthotectonic (metamorphic) zone of Scotland and Donegal, Ireland. *Lithos*, 62, 65–85.
- Aydin, F. (2008). Contrasting complexities in the evolution of calc-alkaline and alkaline melts of the Niğde volcanic rocks, Turkey: textural, mineral chemical and geochemical evidence. *Eur. J. Mineral.*, 20, 101–118.
- Azimzadeh, Z. (2013). *Geochemistry and petrogenesis of Misho Mafic Complex (NW Iran)*. PhD thesis, Tabriz University. pp. 160 (in Persian with English abstract).
- Barrat, J. A., Yamaguchi, A., Greenwood, R. C., Bohn, M., Cotton, J., Benoit, M., and Franchi, I. A. (2007). The Stannern trend eucrites: contamination of main group eucritic magmas by crustal partial melts. *Geochim. Cosmochim. Acta*, 71, 4108–4124.
- Blatter, D. L. and Carmichael, I. S. E. (1998). Hornblende peridotite xenoliths from central Mexico reveal the highly oxidized nature of subarc upper mantle. *Geology*, 26, 1035–1038.
- Boynton, W. V. (1984). Geochemistry of the rare earth elements: meteorite studies. In Henderson, P., editor, *Rare Earth Element Geochemistry*, pages 63–114. Elsevier, Amsterdam.
- Canil, D. and Fedortchouk, Y. (2000). Clinopyroxene-liquid partitioning for vanadium and the oxygen fugacity during formation of cratonic and oceanic mantle lithosphere. *J. Geophys. Res.*, 105, 26003–26016.
- Capedri, S., Venturelli, G., Salvioli, M. E., Crawford, A. J., and Barbieri, M. (1989). Upper-mantle xenoliths and megacrysts in an alkali basalt from Tal-

- lante, south-eastern Spain. *Eur. J. Mineral.*, 1, 685–699.
- Carraro, A. and Visonà, D. (2003). Mantle xenoliths in Triassic camptonite dykes of the Predazzo Area (Dolomites, Northern Italy): petrography, mineral chemistry and geothermobarometry. *Eur. J. Mineral.*, 15, 103–115.
- Corticelli, S., Avanzinelli, R., Poli, G., Braschi, E., and Giordano, G. (2013). Shift from lamproitellike to leucititic rocks: Sr–Nd–Pb isotope data from the Monte Cimino volcanic complex vs. the Vico strato-volcano, Central Italy. *Chem. Geol.*, 353, 246–266.
- Cotten, J. L., Dez, A., Bau, M., Maury, R., Dulsky, P., Fourcade, S., Bohn, M. R., and Brousse, R. (1995). Origin and anomalous rare-earth element and yttrium enrichments in subaerially exposed basalts: evidence from French Polynesia. *Chem. Geol.*, 119, 115–138.
- Cox, K. G., Bell, J. D., and Pankhurst, R. J. (1979). *The Interpretation of Igneous Rocks*. Allen and Unwin, London. page 450.
- Deer, W. A., Howie, R. A., and Zussman, J. (1966). *An Introduction to the Rock Forming Minerals*. Longmans, London. page 528.
- Dehghani, G. A. and Makris, T. (1984). The gravity field and crustal structure of Iran. *Neues Jahrb. Geol. Paläontol. Abh.*, 168, 215–229.
- Deng, J. H., Yang, X. Y., Sun, W. D., Huang, Y., Chi, Y. Y., Yu, L. F., and Zhang, Q. M. (2012). Petrology, geochemistry, and tectonic significance of Mesozoic shoshonitic volcanic rocks, Luzong volcanic basin, eastern China. *Int. Geol. Rev.*, 54, 714–736.
- Dewey, J. F., Hempton, M. R., Kidd, W. S. F., Saroglu, F., and Sengor, A. M. C. (1986). Shortening of continental lithosphere: the neotectonics of Eastern Anatolia—a young collision zone, in collision tectonics. *Geol. Soc. Spec. Publ.*, 19, 3–36.
- Downes, H., Kostoula, T., Iones, P., Beard, D., Thirlwall, F., and Bodinier, L. L. (2002). Geochemistry and Sr–Nd isotopic compositions of mantle xenoliths from the Monte Vulture carbonatite melilitite volcano, central southern Italy. *Contrib. Mineral. Petrol.*, 144, 78–93.
- Downes, H., Upton, B. G. I., Handisyde, E., and Thirlwall, M. F. (2001). Geochemistry of mafic and ultramafic xenoliths from Fidra (Southern Uplands, Scotland): implications for lithospheric processes in Permo-Carboniferous times. *Lithos*, 58, 105–124.
- Emami, H. (1981). *Geologie de la region de Qom-Aran (Iran) contribution a l'etude denamique et geochemique du volcanisme Teriaire del' Iran central*. PhD thesis, University of Grenoble. pp. 513.
- Farhoudi, G. (1978). A comparison of Zagros geology to island arcs. *Geology*, 86, 323–334.
- Frey, F. A. and Prinz, M. (1978). Ultramafic inclusions from San Carlos, Arizona; petrologic and geochemical data bearing on their petrogenesis. *Earth Planet. Sci. Lett.*, 38, 129–176.
- Gertisser, R. and Keller, J. (2000). From basalt to dacite: origin and evolution of the calc alkaline series of Salina, Aeolian Arc, Italy. *Contrib. Mineral. Petrol.*, 139, 607–626.
- Ghasemi, A. and Talbot, C. J. (2006). A new tectonic scenario for the Sanandaj-Sirjan Zone (Iran). *J. Asian Earth Sci.*, 26, 683–693.
- Gill, R. C. O., Aparicio, A., El Azzouzi, M., Hernandez, J., Thirlwall, M. F., Bourgeois, J., and Marriner, G. F. (2004). Depleted arc volcanism in the Alboran Sea and shoshonitic volcanism in Morocco: geochemical and isotopic constraints on Neogene tectonic processes. *Lithos*, 78, 363–388.
- Hammarstrom, J. M. and Zen, E.-a. (1968). Aluminum in hornblende: an empirical igneous geobarometer. *Am. Mineral.*, 719, 1297–1313.
- Hart, S. R., Gerlach, D. C., and White, W. M. (1986). A possible new Sr–Nd–Pb mantle array and consequences for mantle mixing. *Geochim. Cosmochim. Acta*, 50, 1551–1557.
- Hassanzadeh, J. (1993). *Metallogenic and tectonomagmatic events in the SE sector of the Cenozoic active continental margin of Iran (Shahre-Babak area, Kerman Province)*. PhD thesis, University of California, Los Angeles. pp. 204.
- Hofmann, A., Jochum, K., Seufert, M., and White, M. (1986). Nb and Pb in oceanic basalts: new constraints on mantle evolution. *Earth Planet. Sci. Lett.*, 33, 33–45.
- Hofmann, A. W. (1997). Mantle geochemistry: the message from oceanic volcanism. *Nature*, 385, 219–229.
- Hofmann, A. W. and White, W. M. (1982). Mantle plumes from ancient oceanic crust. *Earth Planet. Sci. Lett.*, 57, 421–436.
- Ionov, D. A. and Hofmann, A. W. (1995). Nb–Ta rich mantle amphiboles and mica: implication for subduction-related metasomatic trace element fractionations. *Earth Planet. Sci. Lett.*, 131, 341–

- 356.
- Irving, A. J. and Frey, F. A. (1978). Distribution of trace elements between garnet megacrysts and host volcanic liquids of kimberlitic to rhyolitic composition. *Geochim. Cosmochim. Acta*, 42, 771–787.
- Irving, A. I. (1980). Petrology and geochemistry of composite ultramafic xenoliths in alkalic basalts and implications for magmatic processes within the mantle. *Am. J. Sci.*, 280, 389–426.
- Jahangiri, A. (2007). Post-collisional Miocene adakitic volcanism in NW Iran: geochemical and geodynamic implications. *J. Asian Earth Sci.*, 30, 433–447.
- Keskin, M. (2003). Magma generation by slab steepening and breakoff beneath a subduction-accretion complex: an alternative model for collision-related volcanism in Eastern Anatolia, Turkey. *Geophys. Res. Lett.*, 30, 8046–8050.
- Kheirkhah, M., Allen, M. B., and Emami, M. (2009). Quaternary syn-collision magmatism from the Iran/Turkey borderlands. *J. Volcanol. Geotherm. Res.*, 182, 1–12.
- Kheirkhah, M., Neill, I., and Allen, M. B. (2015). Petrogenesis of OIB-like basaltic volcanic rocks in a continental collision zone: late Cenozoic magmatism of Eastern Iran. *J. Asian Earth Sci.*, 106, 19–33.
- Khezerlou, A., Amini, S., and Moayyed, M. (2008). Petrology, geochemistry and mineral chemistry of potassic and ultrapotassic rocks of North West Marand, NW Iran. *Kharazmi Sci.*, 3, 183–204. (in Persian with English abstract).
- Khezerlou, A., Grégoire, M., Nasir, A., Mohsen, M., Ahmad, J., and Kilzi, M. (2020). Origin and formation process of Gabbro and Diorite Xenoliths in the northern part of Uromieh-Dokhtar Magmatic Belt, NW Iran: constraints from mineral and whole-rock chemistries. *J. Geol.*, 128, 227–246.
- Khezerlou, A., Nasir, A., Grégoire, M., Mohsen, M., and Ahmad, J. (2017). Geochemistry and mineral chemistry of pyroxenite xenoliths and host volcanic alkaline rocks from northwest of Marand (NW Iran). *Mineral. Petrol.*, 111(6), 865–885.
- Kuster, D. and Harms, U. (1998). Post-collisional potassic granitoids from the southern and northern parts of the late neoproterozoic East Africa Orogen: a review. *Lithos*, 45, 177–195.
- Leake, B. E., Woolley, A. R., Arps, C. E. S., Birch, W. D., Gilbert, M. C., Grice, J. D., Hawthorne, F. C., Kato, A., Kisch, H. J., Krivovichev, V. G., Linthout, K., Laird, J., Mandarino, J. A., Maresch, W. V., Nichel, E. H., Rock, N. M. S., Schumacher, J. C., Smith, D. C., Stephenson, N. C. N., Ungaretti, L., Whittaker, E. J. W., and Youzhi, G. (1997). Nomenclature of amphiboles: report of the subcommittee on amphiboles of the International Mineralogical Association, Commission on New Minerals and Mineral Names. *Can. Mineral.*, 35, 219–246.
- Leterrier, J., Maury, R. C., Thonon, P., Girard, D., and Marchal, M. (1982). Clinopyroxene composition as a method of identification of the magmatic affinities of paleo-volcanic series. *Earth Planet. Sci. Lett.*, 59, 139–154.
- Martin, H. (1999). Adakitic magmas: modern analogues of Archaean granitoids. *Lithos*, 46, 411–429.
- Morimoto, N., Fabrice, J., Ferguson, A., Ginzburg, I. V., Ross, M., Seifert, F. A., Zussman, J., Akoi, K., and Gottardi, G. (1988). Nomenclature of pyroxenes. *Mineral. Mag.*, 52, 535–555.
- Morimoto, N. and Kitamura, M. (1983). Q-J diagram for classification of pyroxenes. *J. Jpn. Assoc. Mineral. Petrol. Econ. Geol.*, 78, 132–152. (in Japanese).
- Nachit, H., Ibhi, A., Abia, E. H., and Ohoud, M. B. (2005). Discrimination between primary magmatic biotites, reequilibrated biotites and neofomed biotites. *C. R. Geosci.*, 337, 1415–1420.
- Nicolas, A. (1989). *Structures in Ophiolites and Dynamics of Oceanic Lithosphere*. Kluwer, Dordrecht. page 367.
- Omran, J., Agard, P., Whitechurch, H., Benoit, M., Prouteau, G., and Jolivet, L. (2008). Arc-magmatism and subduction history beneath the Zagros Mountains, Iran: a new report of adakites and geodynamic consequences. *Lithos*, 106, 380–398.
- Orejana, D., Villaseca, C., and Paterson, B. A. (2006). Geochemistry of pyroxenitic and hornblenditic xenoliths in alkaline lamprophyres from the Spanish central system. *Lithos*, 86, 167–196.
- Otten, M. T. (1984). The origin of brown hornblende in the Artfjallet gabbro and dolerites. *Contrib. Mineral. Petrol.*, 86, 189–199.
- Pearce, J. A. and Norry, M. J. (1979). Petrogenetic implications of Ti, Zr, Y, and Nb variations in volcanic rocks. *Contrib. Mineral. Petrol.*, 69, 33–47.
- Pearce, J. A. and Peate, D. W. (1995). Tectonic implications of the composition of volcanic arc magmas. *Annu. Rev. Earth Planet. Sci.*, 23, 251–285.
- Pin, C. and Santos Zalduegui, J. F. (1997). Sequential separation of light rare-earth elements, thorium and uranium by miniaturized extraction



- chromatography: application to isotopic analyses of silicate rocks. *Anal. Chem. Acta*, 339, 79–89.
- Putirka, K. (2016). Amphibole thermometers and barometers for igneous systems, and some implications for eruption mechanisms of felsic magmas at arc volcanoes. *Am. Mineral.*, 101, 841–858.
- Rajabi, S., Torabi, G., and Arai, S. (2014). Oligocene crustal xenolith-bearing alkaline basalt from Jandaq area (Central Iran): implications for magma genesis and crustal nature. *Isl. Arc.*, 23, 125–141.
- Saadat, S. and Stern, C. R. (2012). Petrochemistry of a xenolith bearing neogene alkali olivine basalt from northeastern Iran. *J. Volcanol. Geotherm. Res.*, 225–226, 13–29.
- Saccani, E., Azimzadeh, Z., Dilek, Y., and Jahangiri, A. (2013). Geochronology and petrology of the early carboniferous Misho Mafic complex (NW Iran), and implications for the melt evolution of Paleotethyan rifting in Western Cimmeria. *Lithos*, 162, 264–278.
- Saunders, A. D., Tarney, J., and Weaver, S. D. (1980). Transverse geochemical variations across the Antarctic Peninsula: implications for the genesis of calc-alkaline magmas. *Earth Planet. Sci. Lett.*, 46, 344–360.
- Schweitzer, E. L., Papike, J. J., and Bence, A. E. (1979). Statistical analysis of clinopyroxenes from deep-sea basalts. *Am. Mineral.*, 64, 501–513.
- Sengor, A. M. C. and Kidd, W. S. F. (1979). Post-collisional tectonics of the Turkish–Iranian plateau and a comparison with Tibet. *Tectonophysics*, 55, 361–376.
- Shahzeidi, M. (2013). *Geochemistry and petrology of Misho granitoid from south west marand (NW Iran)*. PhD thesis, Tabriz University. pp. 161 (in Persian with English abstract).
- Sial, A. N., Ferreira, V. P., Fallick, A. E., Jeronimo, M., and Cruz, M. (1998). Amphibole-rich clots in calcalkalic granitoids in the Borborema province northeastern Brazil. *J. South Am. Earth Sci.*, 11, 457–471.
- Sisson, T. W. and Grove, T. L. (1993). Experimental investigation of the role of H<sub>2</sub>O in calc-alkaline differentiation and subduction zone magmatism. *Contrib. Mineral. Petrol.*, 113, 143–166.
- Speer, J. A. (1984). Mica in igneous rocks. In Bailey, S. W., editor, *Micas Rev. Mineral. Geochem.*, volume 13, pages 299–356.
- Stein, E. and Dietl, E. (2001). Hornblende thermometry of granitoids from the central Odenwald (Germany) and their implication for the Geotectoni Development of the Odenwald. *Mineral. Petrol.*, 72(1–3), 185–207.
- Su, B. X., Chung, S. L., Zarrinkoub, M. H., Pang, K. N., Chen, L., Ji, W. Q., Brewer, A., Ying, J. F., and Khatib, M. M. (2014). Composition and structure of the lithospheric mantle beneath NE Iran: constraints from mantlexenoliths. *Lithos*, 202–203, 267–282.
- Sun, S. S. and McDonough, W. F. (1989). Chemical and isotopic systematics of oceanic basalts: implications for mantle composition and processes. In Saunders, A. D. and Norry, M. J., editors, *Magma-tism in the Ocean Basins*, volume 42 of *Geol. Soc. Lond. Spec. Publ.*, pages 313–345. Geological Society, London.
- Turner, S., Arnaud, N., Liu, J., Rogers, N., Hawkesworth, C., Harris, N., Kelley, S., Calsteren, P. V., and Deng, W. (1996). Post-collision, Shoshonitic volcanism on the Tibetan plateau: implications for convective thinning of the lithosphere and the source of ocean island basalts. *J. Petrol.*, 37(1), 45–71.
- Willson, M. (1989). *Igneous Petrogenesis; A Global Tectonic Approach*. Unwin Hyman, London. page 466.
- Witt-Eickschen, G. and Kramm, U. (1998). Evidence for the multiple stage evolution of the subcontinental lithospheric mantle beneath the Eifel (Germany) from pyroxenite and composite pyroxenite peridotite xenoliths. *Contrib. Mineral. Petrol.*, 131, 258–272.
- Wu, L., Guo, X., and Banuelos, G. S. (2003). Selenium and sulfur accumulation and soil selenium dissipation in planting of four herbaceous plant species in soil contaminated with drainage sediment rich in both selenium and sulfur. *Int. J. Phytomed.*, 5, 25–40.
- Yang, J. H., Chung, S. L., Wilde, S. A., Wu, F., Chu, M. F., Lo, C. H., and Fan, H. (2005). Petrogenesis of post-orogenic syenites in the Sulu orogenic belt, East China: geochronological, geochemical and Nd–Sr isotopic evidence. *Chem. Geol.*, 214, 99–125.
- Yousefzadeh, M. and Sabzehei, M. (2012). Thermobarometry of dacites from Markoh (northeast of Birjand) and its amphibolite xenoliths. *Iran. J. Crystallography Mineralogy*, 1, 43–52. (in Persian with English abstract).
- Zhang, H., Zhang, L., Harris, N., Jin, L., and Honglin,

- Y. (2006). U–Pb zircon ages, geochemical and isotopic compositions of granitoids in Songpan-Garze fold belt, eastern Tibetan plateau: constraints on petrogenesis and tectonic evolution of the basement. *Contrib. Mineral. Petrol.*, 152, 75–88.
- Zhang, Y., Yu, K., and Qian, H. (2018). LA-ICP-MS analysis of Clinopyroxenes in Basaltic Pyroclastic Rocks from the Xisha Islands, Northwestern South China Sea. *Minerals*, 8, article no. 575.
- Zindler, A. and Hart, S. R. (1986). Chemical geodynamics. *Annu. Rev. Earth Planet. Sci.*, 14, 493–571.